

SCUOLA INTERNAZIONALE SUPERIORE DI STUDI AVANZATI
INTERNATIONAL SCHOOL FOR ADVANCED STUDIES

Dynamical properties
of
clean and H-covered W(110) surfaces

Thesis submitted for the degree of
“Doctor Philosophiæ”

CANDIDATE

Claudia Bungaro

SUPERVISORS

Prof. Stefano Baroni

Dr. Stefano de Gironcoli

– Trieste, October 1995 –

Table of Contents

Table of Contents	3
Introduction	5
1 Experimental facts	9
2 Theoretical tools	17
2.1 Density-functional theory	18
2.1.1 The local-density approximation	20
2.1.2 The plane-wave pseudopotential approach	21
2.2 Lattice dynamics	25
2.2.1 <i>Ab initio</i> interatomic force constants	27
3 Bulk properties of W	33
3.1 Equilibrium structure	34
3.2 Dynamical properties	36
3.2.1 Real-space interatomic force constants	38

3.2.2	Phonon dispersions	38
4	Clean and hydrogenated W(110) surfaces	41
4.1	Equilibrium structures	42
4.2	Electronic properties	47
4.2.1	Work function	53
4.3	Vibrational properties	57
4.3.1	Clean surface	60
4.3.2	Hydrogenated surface	66
5	Conclusions	73
	Acknowledgments	77
A	Smearing technique in Brillouin-zone integration for metals	79
	Bibliography	83

Introduction

In recent years, the availability of high-resolution surface-sensitive experimental techniques such as Helium atom scattering (HAS) and electron energy loss spectroscopy (EELS) has opened new perspectives in the study of the dynamical properties of solid surfaces. In particular, a great deal of experimental data are now available on the phonon dispersions of surfaces of insulator, semiconductors, and metals [1]. Among transition metals, the vibrational properties of the hydrogenated W(110) surface have attracted much attention because they display unusual and unexpected features which are still poorly understood [2–6]. When a full monolayer of hydrogen is adsorbed, the surface phonon spectrum undergoes a dramatic change and an anomalous behavior appears. The phonon dispersion curves observed in HAS experiments display a shallow dip and a very sharp and deeper indentation at an incommensurate wave vector along the [001] direction ($\overline{\Gamma\text{H}}$), whereas only the shallow dip is observed by EELS. The anomaly is a peculiar feature of the hydrogen saturated surface: a regular behavior of the phonon dispersions has been detected at lower coverage and for the clean surface. Similar anomalies have been also found in the H-saturated Mo(110) surface [4, 5]. The two surfaces W(110) and Mo(110)

have analogous electronic structure and display similar properties.

Phonon anomalies similarly deep and strongly localized in reciprocal space had only been previously observed in quasi one-dimensional conductors [7, 8]. These giant Kohn anomalies are known to be caused by a strong electron-phonon coupling, kinematically enhanced by the presence of extended parallel sections in the quasi one-dimensional Fermi surface (“nesting”). Angular-resolved photo-emission studies on H/W(110) and H/Mo(110) gave no evidence of similar nesting features in the two-dimensional Fermi surfaces [9]. With the exception of W(100) and Mo(100) [10, 11] no other cases are known of strong Kohn anomalies observed in the phonon dispersions of crystal surfaces. Therefore the appearance of these anomalous features in the surface scattering experiments on H/W(110) and H/Mo(110) is surprising and raises much interest and many questions. In particular, it is difficult to reconcile the different pieces of experimental information: the presence of the huge dip in the HAS spectra which are missing in the surface phonon dispersions measured by EELS; the finding of a phonon anomaly, but the absence of corresponding nesting features in the experimental Fermi surface contours.

So far no exhaustive explanations of these anomalies has been put forward. In particular, no detailed theoretical studies of the vibrational properties of these surfaces are available. In this thesis we present the results of an *ab initio* study of the structural, electronic, and vibrational properties of the clean and hydrogen-saturated W(110) surfaces. Our calculations are based on density functional theory (DFT) and density functional perturbation theory (DFPT). An accurate study of the surface phonon dispersions for the H/W(110) surface allows us to ascertain the

existence of Kohn anomalies, and to clarify the nature of the the anomalous features observed experimentally. The electronic properties at the Fermi level are investigated in order to determine the existence of nesting properties in the Fermi surface that can play an important role in the appearance of phonon anomalies.

The vibrational properties of a surface are determined by the force constants between atoms near it. The surface interatomic force constants are different from those in the bulk due to the lower atom coordination and to changes both in the local atomic structure and in the electronic states near the surface. For this reason semiempirical models, which are usually fitted to some observed lattice-dynamical properties of the bulk, are expected to have a rather limited predictive power, and the use of more sophisticated *ab initio* techniques based on a proper quantum description of the electronic glue are called for.

DFPT provides a general theoretical and computationally viable tool for obtaining the harmonic force constants of complex systems fully *ab initio* without the use of any adjustable parameter. This method—which is based on the static linear response of electrons to lattice distortions—gives access to the phonon frequencies and the corresponding atomic displacement patterns at any point in the Brillouin zone (BZ), allowing us to calculate full phonon dispersions even at incommensurate points in the BZ. This technique has been successfully applied to predict vibrational and related properties of elemental and binary semiconductors [12] or insulators [13], semiconductor alloys [14] and eterostructures [15], and more recently to the calculation of phonon dispersions in bulk metals [16] and semiconductor surfaces [17].

The first Chapter of this thesis is devoted to review the experimental character-

ization of the studied surfaces. In particular the experimental data concerning the phonon anomalies are summarized, and the different possible scenarios proposed to explain them are discussed. In Chapter 2 we briefly discuss the theoretical tools used in this work, namely DFT and DFPT. Our results on the structural and vibrational properties of bulk W are presented in Chapter 3, while Chapter 4 is devoted to a detailed description of the structural, electronic, and vibrational properties of the clean and hydrogen saturated W(110) surfaces. The last chapter is devoted to our conclusions and the perspectives for future work.

Chapter 1

Experimental facts

Tungsten is a transition metal which crystallizes in the bcc structure. Its (110) surface is unreconstructed with less than 2% relaxation in the first intra-layer distance [18]. The phase diagram of adsorbed hydrogen on W(110) is well known [19]: at low temperature several ordered phases have been found for different coverages: below half a monolayer the surface reconstructs as (2×1) , while a (2×2) reconstruction arises at higher coverages. These structures disorder at temperatures above 200 and 250 K, respectively. As a full monolayer is adsorbed, the (1×1) periodicity of the clean surface is recovered. For H-coverages exceeding half a monolayer a symmetry loss in the low energy electron diffraction (LEED) pattern has been observed at low and room temperature [20]. This has been interpreted as an adsorbate induced “reconstruction”, which consists in a lateral shift of the topmost layer of W atoms in the $[1\bar{1}0]$ direction, thus implying that the reflection symmetry about the $[1\bar{1}0]$ plane would be lost (though preserving the translational periodicity). EELS measurements suggest that the hydrogen atom is bonded in the hollow site above

the hourglass-shaped hole between the tungsten atoms in the surface layer [21].

The vibrational properties of the clean and hydrogenated W(110) surfaces have been studied both by HAS [2–5] and by EELS [6]. For the clean surface two surface phonon modes have been detected by both techniques along the symmetry lines $\overline{\Gamma\text{H}}$, $\overline{\Gamma\text{N}}$ and $\overline{\Gamma\text{S}}$ in the two-dimensional surface Brillouin zone (SBZ). The lowest branch is the Rayleigh wave (RW) mode falling below the frequency region allowed to bulk phonons. The second mode, which lie within the bulk band, has been interpreted as the longitudinally polarized surface mode. Two other surface resonances have been observed by EELS at higher frequencies (at about 160 and 190 cm^{-1} respectively).

When the W(110) surface is covered by a full monolayer of hydrogen, the RW branch along the [001] direction ($\overline{\Gamma\text{H}}$) presents an unexpected anomalous behavior (see Fig. 1.1). An extremely deep and sharp indentation and a more shallow dip at the incommensurate wave vector $q_{c1}=0.95 \text{ \AA}^{-1}$ are observed in HAS experiments [3, 4]; with EELS, instead, only the shallow dip is observed (see Fig. 1.2). The anomalies have been found by HAS also at the commensurate zone boundary point $q_{c2}=\overline{\text{S}}$ along the $[1\overline{1}2]$ direction [3],¹ where the RW dispersion shows a shallow dip and a less clearly visible deeper indentation. EELS data along this direction are not available. The observed anomalies are peculiar features of the H-saturated phase: surface phonons at lower coverages (corresponding to the (2×1) and (2×2) reconstructions) display smooth dispersion curves and back folding due to the reduced size of the BZ's in the reconstructed structures.

The explanation of such anomalies is a puzzling problem, and different scenarios

¹Note that the $[1\overline{1}2]$ has been erroneously labeled $[1\overline{1}1]$ in Ref.[3].

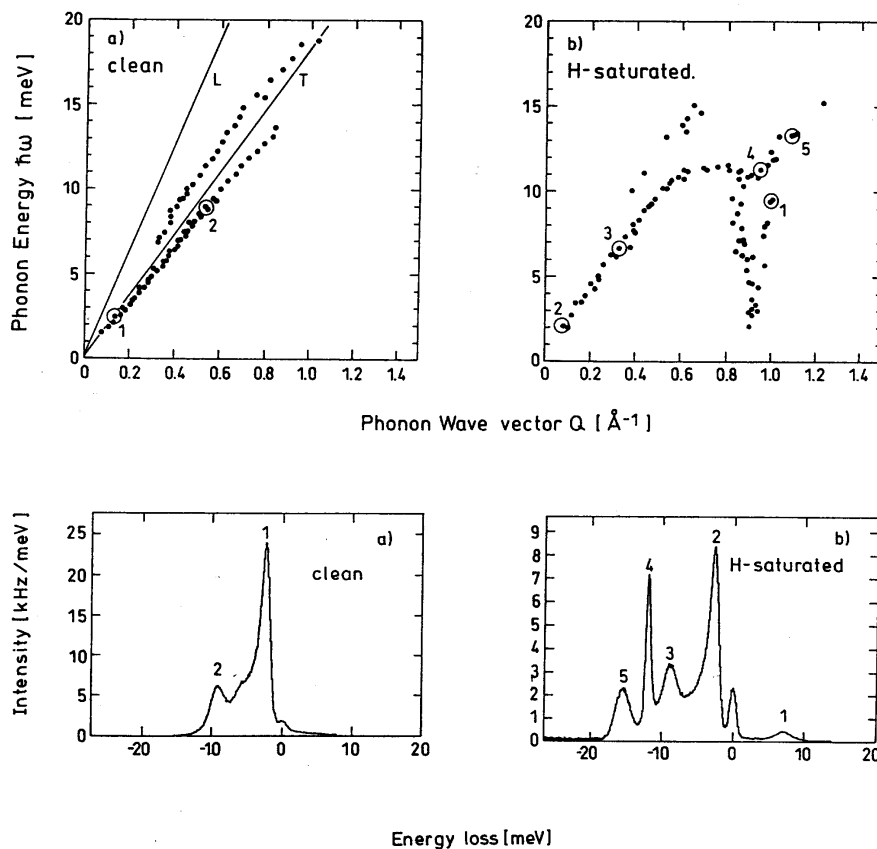


Figure 1.1: He-atom scattering spectra of clean (left panels) and H-saturated (right panels) W(110) surface phonon along the [001] direction. The upper panel on the left shows the surface phonon dispersion data for the clean surface. The solid lines in represent the lower edges of the transverse (T) and longitudinal (L) bulk phonon bands. The upper panel on the right shows the surface phonon dispersion data for the H/W(110) surface, the phonon softening occurs at $q_c=0.95 \text{ \AA}^{-1}$. Typical spectra are shown in the lower panels, the labels on the peaks refers to points in the respective surface phonon dispersion. (Fig. from Ref.[4]).

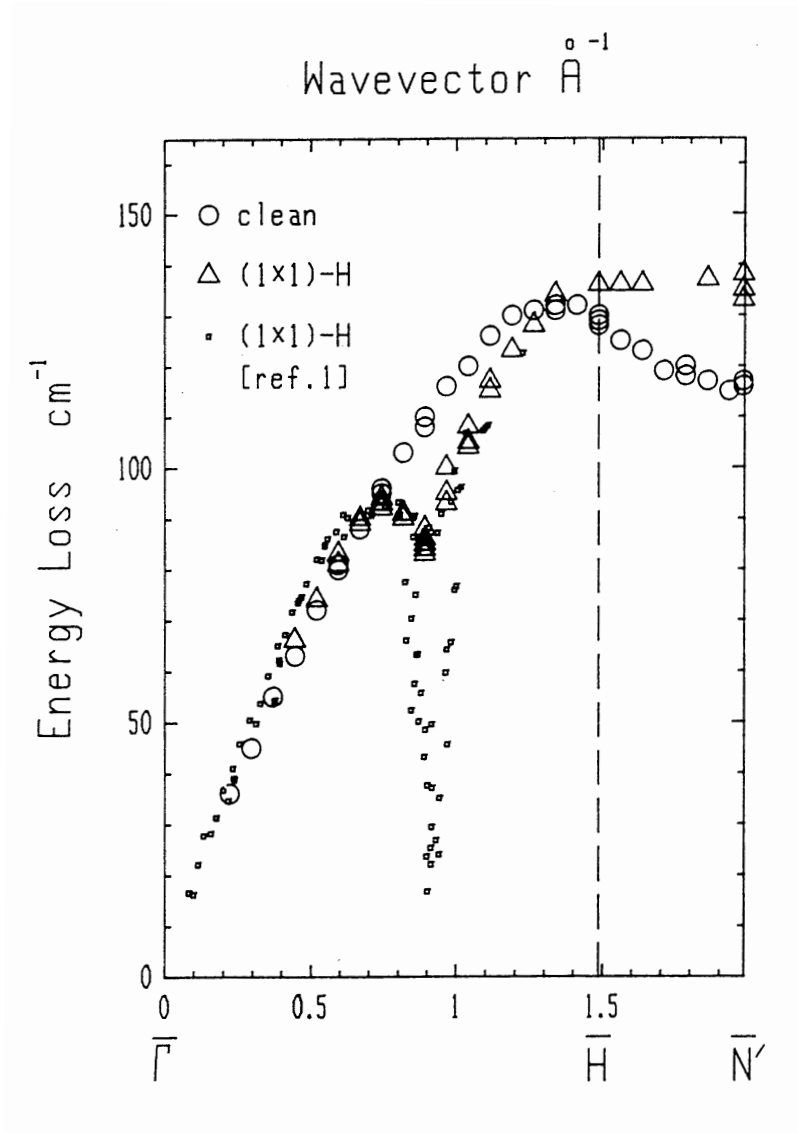


Figure 1.2: Experimental surface phonon dispersion curves of the W(110) surfaces (from Ref. [6]). The big symbols indicate EELS data of the clean (circles) and H-saturated (triangles) surface. The small squares are the HAS data for the H-saturated surface.

have been proposed. The agreement between the HAS and EELS dispersion curves supports the idea that the shallow indentation is associated to an anomaly of the RW branch. The interpretation of the second huge and sharp dip, not found in the EELS experiments, is less straightforward.

In Ref. [22], it was proposed that the anomalous mode is associated to the motion of hydrogen atoms to which electrons are less sensitive than He atoms. In particular the authors identify the deep minimum with roton-like excitations of the H-overlayer found to be in a disordered, possibly liquid-like, state. However no direct link with H-vibrations has been observed, the dispersions staying unchanged when deuterium is adsorbed instead of hydrogen [5]. We conclude that the effect of the (D) H overlayer on W vibrations is indirect and should be mediated by the modification of the chemical and electronic properties occurring in the substrate.

Other possible explanations have been suggested by the resemblance between the deep indentation and phonon anomalies observed in quasi one-dimensional conductors [7]. In these systems the electron-phonon (e-ph) coupling is kinematically enhanced by the presence of extended parallel portions of the Fermi surface, nested by a critical wave vector $\mathbf{q}_c = 2\mathbf{k}_F$. This gives rise to strong electronic screening at $\mathbf{q} = \mathbf{q}_c$ which strongly reduces the atomic force constants. Thus a so called giant Kohn anomaly occurs in the phonon dispersion at the nesting wave vector. Within this picture the two anomalous mode in the HAS spectra would be explained if a second mode, at higher frequencies, were softened together with the RW mode. This explanation seems to be ruled out by the fact that the lower surface branch is not visible in EELS experiments.

If the e-ph coupling and the Kohn anomaly become very strong, the anomalous frequency becomes imaginary and the system unstable. A stabilizing distortion would take place, inducing a charge-density wave (CDW). The hypothesis that the ground state of the H/W(110) surface is a quasi one-dimensional CDW, incommensurate along $\overline{\Gamma\text{H}}$ and commensurate along $\overline{\Gamma\text{S}}$ has been suggested in reference [23] in which it has been proposed that the lower and upper anomalous branches are the phase and amplitude modes of the CDW, respectively. If this picture were correct and the lower anomalous branch a phason, it would be detected by HAS, that is sensitive to the corrugation of the electronic charge density on the surface, but not by EELS because the electrons are scattered by the cores of the surface atoms. This would be in agreement with the difference between the spectra observed by the two experimental techniques. Nevertheless such a phason could exist at an incommensurate point like q_{c1} , but it should be absent at the zone boundary commensurate point q_{c2} [24] contrary to the experimental evidence. Furthermore, the frequency of CDW modes decreases with increasing temperature ($d\omega/dT < 0$); on the contrary, these anomalous frequencies were found to be independent on temperature [4, 5], and recent EELS experiments reveal a slight positive temperature dependence of the shallow dip ($d\omega/dT > 0$), consistent with the behavior expected of a Kohn anomaly.

Another interpretation of the experimental data assumes that e-ph coupling and the associated Kohn anomaly are only moderate, and the unreconstructed surface structure remains therefore stable. Within this picture electron-hole pair excitations and phonons become mixed in character and the adiabatic approximation is broken. One should then expect a predominantly phonon-like excitation resulting in a slight

softening of the phonon frequency, that can be identified with the shallow dip observed in the RW branch. A predominantly electron-hole like excitation should be expected at very low energy in agreement with the huge indentation detected by the HAS scattering. This would explain the absence of the lower anomaly in the EELS spectra which are not sensitive to charge corrugations on the surface. The agreement of the experimental data and a frozen phonon calculation of the RW frequency performed at the commensurate zone boundary \bar{S} point [25] seems to support the identification the shallow dip with a softening of the RW mode.

The idea that the origin of the surface anomalies is a nesting mechanism at the Fermi surface is apparently not consistent with angular-resolved photoemission studies that do not provide any evidences of nesting in the two-dimensional Fermi surface (FS) of the H/W(110) [9]. The shape of the experimental Fermi surfaces disagrees with the results of recent calculations showing nesting features in fair agreement with what would be expected to explain the phonon anomalies [26, 25].

Chapter 2

Theoretical tools

The study of the structural, electronic and vibrational properties of the systems investigated in this thesis, has been performed within *ab initio* methods based on density-functional theory. At zero temperature, the properties we are interested in can be determined starting from the knowledge of the quantum-mechanical electronic ground-state. From a microscopic point of view, a crystal is a system of ions and electrons interacting through Coulomb forces. In the spirit of the Born-Oppenheimer (or *adiabatic*) approximation [27], the electronic degrees of freedom can be decoupled from the nuclear ones. Within this approximation, based on the large difference between the electronic and the nuclear masses, the electrons are assumed to follow adiabatically the ionic motion, remaining very close to their instantaneous ground-state configuration. The electrons are described by a Schrödinger equation where the ions act as fixed potential sources. On the other hand, the dynamics of the ions can be studied as if they were classical charged particles, moving in the *effective potential* determined by the electronic ground-state energy which

depends parametrically on the nuclear positions. DFT provides a theoretical framework to describe the electronic ground-state of a solid, without having to solve the Schrödinger equation for the quantum many-electron system, which would be an impossible task due to the very large number of degrees of freedom involved in the calculation.

2.1 Density-functional theory

The density-functional theory is based on the Hohenberg-Kohn theorem [28] which states that the external potential acting on the electrons is uniquely determined by the ground-state electronic density $n(\mathbf{r})$. This potential, in turn, yields in principle the ground-state wave-function that determines all the other ground-state properties of the system, which result therefore to be functionals of $n(\mathbf{r})$. In particular, for a given external potential $V_{\text{ext}}(\mathbf{r})$, it is possible to define the energy functional as follows:

$$E^{el}[V_{\text{ext}}, n] \equiv \int V_{\text{ext}}(\mathbf{r})n(\mathbf{r})d\mathbf{r} + F[n], \quad (2.1)$$

where $F[n]$ is a universal functional of $n(\mathbf{r})$ (i.e. independent on $V_{\text{ext}}(\mathbf{r})$) whose form is however in general unknown. The energy functional plays a central role because it is minimized by the ground-state electronic charge density, under the constraint that the number of electrons N is fixed:

$$E_0 = \min_n (E^{el}[V_{\text{ext}}, n]), \quad (2.2)$$

$$\int n(\mathbf{r})d\mathbf{r} = N, \quad (2.3)$$

and the value at the minimum corresponds to the ground-state energy E_0 . The problem of determining the ground-state energy and charge density is now reduced to the one of minimizing a functional of $n(\mathbf{r})$ whose form is however unknown. The Kohn and Sham [29] idea is to recast this functional separating out of it a term, $T_0[n]$, defined as the kinetic energy of a non interacting electron system of density $n(\mathbf{r})$, and the Hartree term, which is the classical electrostatic interaction between the electrons:

$$F[n] = T_0[n(\mathbf{r})] + \int \frac{n(\mathbf{r})n(\mathbf{r}')}{|\mathbf{r} - \mathbf{r}'|} d\mathbf{r}d\mathbf{r}' + E_{xc}[n(\mathbf{r})]. \quad (2.4)$$

All our ignorance is now confined to the exchange-correlation energy, $E_{xc}[n(\mathbf{r})]$, defined by the Eq. 2.4 as the difference between the unknown functional $F[n]$ and the known terms in its right hand side. Following this approach, the minimization of the total energy functional $E[n]$ results in a set of self-consistent single-particle equations:

$$\underbrace{[-\nabla^2 + V_{\text{SCF}}(\mathbf{r})]}_{H_{KS}} \psi_i(\mathbf{r}) = \epsilon_i \psi_i(\mathbf{r}), \quad (2.5)$$

$$V_{\text{SCF}}(\mathbf{r}) = V_{\text{ext}}(\mathbf{r}) + 2 \int \frac{n(\mathbf{r}')}{|\mathbf{r} - \mathbf{r}'|} d\mathbf{r}' + v_{xc}(\mathbf{r}), \quad (2.6)$$

$$n(\mathbf{r}) = \sum_i |\psi_i(\mathbf{r})|^2 \theta(\epsilon_i - \epsilon_F). \quad (2.7)$$

These are the well known Kohn-Sham (KS) equations, where the Fermi energy ϵ_F is defined by the condition on the number of electrons, Eq. 2.3, $v_{xc}(\mathbf{r}) \equiv \delta E_{xc}[n]/\delta n(\mathbf{r})$ is the exchange-correlation potential, and the single-particle orbitals satisfy the orthonormality constraints $\int \psi_i^*(\mathbf{r})\psi_j(\mathbf{r})d\mathbf{r} = \delta_{ij}$. For electrons in a crystal the external potential is generated by the ionic cores: $V_{\text{ext}}(\mathbf{r}) = V_{\text{ion}}(\mathbf{r})$. In Eqs. 2.4–2.7, as well

as in the rest of this thesis, we have used atomic units: $e^2/2 = \hbar = 2m_e = 1$ (the energy is measured in Rydberg units).

2.1.1 The local-density approximation

The solution of the Kohn-Sham equations gives in principle the ground-state density and energy, but a practical implementation of it is impossible unless an approximation to the unknown exchange-correlation potential is specified. The most used approximation is the so-called local density approximation (LDA), which assumes that at each point \mathbf{r} the exchange-correlation energy density is that of a uniform electron gas whose density is equal to the local density $n(\mathbf{r})$:

$$E_{xc}^{LDA}[n] = \int n(\mathbf{r})\epsilon_{xc}(n(\mathbf{r}))d\mathbf{r}, \quad (2.8)$$

where $\epsilon_{xc}(n)$ is the exchange-correlation energy per particle of the electron gas with uniform density n . The exchange-correlation potential is written in LDA as:

$$v_{xc}(\mathbf{r}) \equiv \frac{\delta E_{xc}[n]}{\delta n(\mathbf{r})} = \frac{d}{dn} (n\epsilon_{xc}(n)) \Big|_{n=n(\mathbf{r})} \equiv \mu_{xc}(n(\mathbf{r})). \quad (2.9)$$

Once the KS equations are solved, the ground-state total energy of the crystal can be written as:

$$\begin{aligned} E^{tot} &= E^{el}[V_{ion}, n] + E^{ion} \\ &= -\sum_i \theta(\epsilon_i - \epsilon_F) \int \psi_i^*(\mathbf{r}) \nabla^2 \psi_i(\mathbf{r}) d\mathbf{r} + \int V_{ion}(\mathbf{r}) n(\mathbf{r}) d\mathbf{r} \\ &+ \int \frac{n(\mathbf{r})n(\mathbf{r}')}{|\mathbf{r} - \mathbf{r}'|} d\mathbf{r} d\mathbf{r}' + \int n(\mathbf{r})\epsilon_{xc}(n(\mathbf{r}))d\mathbf{r} \\ &+ \sum_{\mathbf{R}, s, s'}' \frac{Z_s Z_{s'}}{|\mathbf{R} + \tau_s - \tau_{s'}|}, \end{aligned} \quad (2.10)$$

where the last term, E^{ion} , is the Coulomb interaction between the ionic charges Z_s , the vector \mathbf{R} runs over the direct lattice, τ_s indicates the different atomic positions within the unit cell of the crystal, and the prime indicates that the $\mathbf{R} + \tau_s - \tau'_s = 0$ term has to be omitted from the sum. The total energy, E^{tot} , depends parametrically on the ionic position ($\mathbf{R} + \tau_s$). The dependence is explicit through the ionic Coulomb interaction E^{ion} and the ionic potential $V_{ion}(\mathbf{r})$, and implicit through the electron density $n(\mathbf{r})$ and orbitals $\psi_i(\mathbf{r})$.

2.1.2 The plane-wave pseudopotential approach

To solve in practice the Kohn-Sham equations, one usually expresses the KS orbitals in terms of a suitable finite basis set. When plane-waves (PW) are chosen, taking advantage of the translational invariance and the resulting Bloch theorem, the KS orbitals can be expanded as follows:

$$\psi_i(\mathbf{r}) = \psi_{n,\mathbf{k}}(\mathbf{r}) = \sum_{\mathbf{G}} e^{i(\mathbf{k}+\mathbf{G})\mathbf{r}} c_{n\mathbf{k}}(\mathbf{G}), \quad (2.11)$$

where \mathbf{k} belongs to the first Brillouin Zone of the crystal, \mathbf{G} is a reciprocal lattice vector, and n is the band index. The dimension of the PW basis set is determined by fixing the kinetic energy cutoff, E_{cut} , through the condition:

$$|\mathbf{k} + \mathbf{G}|^2 \leq E_{cut}. \quad (2.12)$$

The choice of a PW basis has the advantage that the matrix elements of the Hamiltonian in Eq. 2.5 are particularly simple and that the accuracy of the expansion can be easily checked and systematically improved by increasing the value of E_{cut} . Furthermore, PW's are independent of the structure of the crystal, and allow a simple

solution of the Poisson equation 2.6. The number N_{pw} of plane waves is related to the energy cutoff by the relationship:

$$N_{pw} \approx \frac{4\pi}{3\Omega_{BZ}} (E_{\text{cut}})^{\frac{3}{2}}, \quad (2.13)$$

where Ω_{BZ} is the volume of the BZ.

If all the electrons were treated explicitly, a huge number of PW's would be necessary to describe the strongly localized core electrons and the rapid oscillations of the valence wave functions in the core region. In order to obtain an accurate description of the system with a reasonably small number of PW's the core electrons are frozen in the atomic configuration around the nuclei, and only the chemically active valence electrons are treated explicitly. To this end, a smooth angular-momentum-dependent *pseudopotential* is then introduced to describe the interaction between valence electrons and ionic cores (nuclei + core electrons). There are many different schemes to generate ionic pseudopotentials from first-principles (see for example [30–33]). Basically, all of them satisfy the following requirements: (i) the lowest pseudo-energy levels are equal to the valence all-electron energies; (ii) each pseudo-wave function coincides with the corresponding all-electron one outside a properly chosen core radius; (iii) as a consequence of (ii), the real and pseudo charge inside the core radius agree for each valence state. This last condition is called *norm conservation*, and ensures the transferability of the pseudopotential to different chemical environments. The accuracy of the results obtained with *norm-conserving* pseudopotentials is comparable with those from all-electron calculations [34, 35].

The usual form for the pseudopotential is semilocal (SL), i.e. it is local with

respect to the radial coordinate and non-local with respect to the angular ones:

$$v_s^{(SL)}(\mathbf{r}, \mathbf{r}') = v_s^{\text{loc}}(r)\delta(\mathbf{r} - \mathbf{r}') + \sum_{l=0}^{l_{\max}} v_{sl}(r)\delta(r - r')P_l(\hat{\mathbf{r}}, \hat{\mathbf{r}}') \quad , \quad (2.14)$$

where the index s refers to the atomic species. The non-locality arises from the projector P_l on the angular momentum l , defined as:

$$P_l(\hat{\mathbf{r}}, \hat{\mathbf{r}}') = \sum_{m=-l}^l Y_l^m(\theta, \phi)Y_l^{*m}(\theta', \phi'), \quad (2.15)$$

Y_l^m 's being normalized spherical harmonics.

A computationally convenient form for the ionic pseudopotential has been introduced by Kleinman and Bylander (KB) [36]. They pointed out that a significant reduction of the numerical effort can be achieved if the non locality of the potential is not restricted to the angular part, as in Eq. 2.14, but if also the radial potential is replaced by a suitable non local separable operator. With the following substitution:

$$v_{sl}(r)\delta(r - r') \longrightarrow \frac{v_{sl}(r)R_{sl}(r)R_{sl}(r')v_{sl}(r')}{\langle R_{sl}|v_{sl}|R_{sl} \rangle}, \quad (2.16)$$

where $R_{s,l}(r)$ is the radial pseudo-wave function, the SL potential in Eq. 2.14 becomes a separable operator defined as follows:

$$v_s^{(KB)}(\mathbf{r}, \mathbf{r}') = v_s^{\text{loc}}(r)\delta(\mathbf{r} - \mathbf{r}') + \sum_{l=0}^{l_{\max}} \sum_{m=-l}^l \varphi_{slm}^{(KB)}(r)\varphi_{slm}^{*(KB)}(r'), \quad (2.17)$$

The computational cost for the application of the KS Hamiltonian in reciprocal space, (i.e. for the calculation of the $H_{KS}|\psi_i\rangle$ product), is proportional to N_{pw}^2 if the SL form is used, and scales as $N_{pw}N_{at}$ when the potential is in the KB form (where N_{at} is the number of atoms in the unit cell of the crystal). It is to be noted

that all the other terms in the Hamiltonian are local either in the reciprocal space (kinetic energy) or in the real space, and their application needs a computational effort proportional to N_{pw} , while passing from a representation to the other through fast Fourier transform costs $\approx N_{pw} \log N_{pw}$. For a given value of E_{cut} , the number of PW's scales as Ω_{BZ}^{-1} , i.e. as the volume of the unit cell of the system $\Omega = (2\pi)^3 \Omega_{BZ}^{-1}$, that is in turn proportional to N_{at} . The KB form must be used with some caution because in some cases it can lead to a wrong description of the chemical properties of the system, due to the appearance of unphysical states in the energy spectrum of the isolated atom. These spurious states, known in the literature as *ghosts* [37], may occur below or immediately above the physically relevant valence states because—due to the non locality of the radial potential—it is no longer guaranteed that the radial wave-functions can be ordered in terms of the increasing number of their nodes. As discussed in Ref. [37], a slight modification of the l -dependent part of the pseudopotential $v_{sl}^{(SL)}(r)$, and/or a judicious choice of the reference local potential are often sufficient to remove the ghosts. We rewrite the potential in the following form:

$$\begin{aligned}
 v^{(SL)}(\mathbf{r}, \mathbf{r}') &= (v^{\text{loc}}(r) + v_{l^*}(r)) \delta(\mathbf{r} - \mathbf{r}') \\
 &+ \sum_{l=0}^{l_{\text{max}}} \underbrace{(v_l(r) - v_{l^*}(r))}_{\Delta V_l(r)} \delta(r - r') P_l(\hat{\mathbf{r}}, \hat{\mathbf{r}}')
 \end{aligned} \tag{2.18}$$

where the non local potential $v_{l^*}(r)$ corresponding to $l = l^*$, is used as a reference. The potential in this form is equivalent to 2.14 for any choice of l^* between zero and l_{max} , with the only difference that now the potential seen by angular momenta larger than l_{max} is $(v^{\text{loc}}(r) + v_{l^*}(r))$ instead of $v^{\text{loc}}(r)$. By changing the choice of l^* it

is often possible to modify $\Delta V_i(r)$ in order to eliminate the presence of *ghost* states.

2.2 Lattice dynamics

Phonons are normal modes of the harmonic lattice vibrations. Within the *adiabatic* approximation, the lattice dynamics can be studied as if the ions were classical charges moving in an effective potential determined by the ground-state electronic energy. Therefore the total energy 2.10, as a function of all nuclear coordinates, plays the role of a potential surface for the atomic motion. For small displacements of atoms around their equilibrium positions, $\mathbf{u}_s(\mathbf{R})$, the total energy of the crystal can be expanded in a Taylor series, which up to second order would read:

$$E^{tot}[\mathbf{u}] = E_0^{tot} + \frac{1}{2} \sum_{\mathbf{R}, \mathbf{R}', s, s'} \frac{\partial^2 E^{tot}}{\partial \mathbf{u}_s(\mathbf{R}) \partial \mathbf{u}_{s'}(\mathbf{R}')} \mathbf{u}_s(\mathbf{R}) \mathbf{u}_{s'}(\mathbf{R}') + \mathcal{O}(\mathbf{u}^3). \quad (2.19)$$

The linear terms vanish because of equilibrium. E_0^{tot} is the total energy of the crystal at equilibrium, and $\mathbf{u}_s(\mathbf{R})$ is the displacement of the s -th atom in the unit cell located at \mathbf{R} . Within this picture, the harmonic oscillations around equilibrium positions are governed by the equations of motion:

$$M_s \ddot{u}_{\alpha s}(\mathbf{R}) = - \frac{\partial E^{tot}}{\partial u_{\alpha s}(\mathbf{R})} = - \sum_{\mathbf{R}', s', \beta} C_{\alpha s, \beta s'}(\mathbf{R} - \mathbf{R}') u_{\beta s'}(\mathbf{R}'). \quad (2.20)$$

where M_s is the mass of the s -th atom, and $\alpha, \beta = x, y, z$ are the polarizations.

The interatomic force constants $C_{\alpha s, \beta s'}(\mathbf{R} - \mathbf{R}')$ are given by:

$$C_{\alpha s, \beta s'}(\mathbf{R} - \mathbf{R}') = \left. \frac{\partial^2 E^{tot}}{\partial u_{\alpha s}(\mathbf{R}) \partial u_{\beta s'}(\mathbf{R}')} \right|_0, \quad (2.21)$$

where the second derivatives are calculated at equilibrium. $C_{\alpha s, \beta s'}(\mathbf{R} - \mathbf{R}')$ represents the negative of the linear force on atom s in the cell at \mathbf{R} along the α direction due

to a unit displacement of atom s' in the cell at \mathbf{R}' along the β direction. The force constants are connected to each other by relations due to the symmetry properties of the crystal. In particular they only depend on the difference $(\mathbf{R} - \mathbf{R}')$ because of the translational invariance of the crystal. Thanks to translational invariance, the solutions of the infinite set of coupled equations 2.20 are Bloch-waves:

$$\mathbf{u}_s(\mathbf{R}) = \frac{1}{\sqrt{M_s}} \mathbf{u}_s(\mathbf{q}) e^{i\mathbf{q}\mathbf{R} - i\omega t}, \quad (2.22)$$

where the wave vector \mathbf{q} belongs to the Brillouin zone. Once the dynamical matrix is known, the problem of solving the lattice dynamics is reduced to a $3N_{at} \times 3N_{at}$ eigenvalue problem:

$$\omega^2 \mathbf{u}_s(\mathbf{q}) = \sum_{s'} \mathbf{D}_{ss'}(\mathbf{q}) \mathbf{u}_{s'}(\mathbf{q}). \quad (2.23)$$

The *dynamical matrix* $\mathbf{D}_{ss'}(\mathbf{q})$ is related to the Fourier transform of the matrix of force constants :

$$D_{\alpha s, \beta s'}(\mathbf{q}) = \frac{1}{\sqrt{M_s M_{s'}}} \sum_{\mathbf{R}} C_{\alpha s, \beta s'}(\mathbf{R}) e^{-i\mathbf{q}\mathbf{R}}. \quad (2.24)$$

It is a hermitian matrix, and has the well known properties [38]:

$$D_{\alpha s, \beta s'}(\mathbf{q}) = D_{\beta s', \alpha s}^*(\mathbf{q}), \quad D_{\alpha s, \beta s'}(-\mathbf{q}) = D_{\alpha s, \beta s'}^*(\mathbf{q}). \quad (2.25)$$

For each \mathbf{q} point in the BZ, the $3N_{at}$ eigenvalues of the dynamical matrix: $\omega_\nu^2(\mathbf{q})$; $\nu = 1, 2, \dots, 3N_{at}$, are positive for stable systems. Their square root gives the frequency of the ν -th vibrational normal-mode, i.e. the dispersion relations $\omega = \omega_\nu(\mathbf{q})$. The corresponding $3N_{at}$ eigenvectors $\mathbf{u}_s^\nu(\mathbf{q})$ are related to the normal-mode atomic displacements through the Eq. 2.22. Every harmonic vibration of the lattice is a linear superposition of the $3N_{at}$ normal-modes.

2.2.1 *Ab initio* interatomic force constants

A complete description of the harmonic vibrations of a crystal is provided by the knowledge of the interatomic force constants. Within the adiabatic approximation, the lattice distortion associated with a phonon can be seen as a static perturbation acting on the electrons. Furthermore, it is well known that the linear variation of the electron density upon application of an external, static, perturbation determines the energy variation up to second order in the perturbation (up to third order, indeed, as stated by the “ $(2n+1)$ theorem” [39]). When the external perturbation is due to ionic displacements, this allows one to calculate the interatomic force constants which are directly obtained from the electronic linear-response to ionic displacements. In fact, the *bare* ionic (pseudo-)potential acting on the electrons is a continuous function of the atomic displacements $\mathbf{u} \equiv \{\mathbf{u}_s(\mathbf{R})\}$. The electronic contribution to the force associated with the displacement along α of the s -th ion in the cell at \mathbf{R} ($u_{\alpha s}(\mathbf{R})$) is given by the Hellmann-Feynman theorem [40]:

$$\frac{\partial E_{[\mathbf{u}]}^{el}}{\partial u_{\alpha s}(\mathbf{R})} = \int n_{[\mathbf{u}]}(\mathbf{r}) \frac{\partial V_{[\mathbf{u}]}^{ion}(\mathbf{r})}{\partial u_{\alpha s}(\mathbf{R})} d\mathbf{r}, \quad (2.26)$$

where $E_{[\mathbf{u}]}^{el}$ is the electronic ground-state energy relative to given values of the atomic displacements \mathbf{u} , and $n_{[\mathbf{u}]}$ is the corresponding electron-density distribution. The electronic contribution to the harmonic force constants is then obtained by differentiating Eq. 2.26 with respect to $\mathbf{u}_{s'}(\mathbf{R}')$:

$$\frac{\partial^2 E_{[\mathbf{u}]}^{el}}{\partial u_{\beta s'}(\mathbf{R}') \partial u_{\alpha s}(\mathbf{R})} = \int \left(\frac{\partial n_{[\mathbf{u}]}(\mathbf{r})}{\partial u_{\beta s'}(\mathbf{R}')} \frac{\partial V_{[\mathbf{u}]}^{ion}(\mathbf{r})}{\partial u_{\alpha s}(\mathbf{R})} + n_0(\mathbf{r}) \frac{\partial^2 V_{[\mathbf{u}]}^{ion}(\mathbf{r})}{\partial u_{\alpha s}(\mathbf{R}) \partial u_{\beta s'}(\mathbf{R}')} \right) d\mathbf{r}, \quad (2.27)$$

where all the derivatives are calculated at the equilibrium positions, i.e. at $\mathbf{u} = \mathbf{0}$, $n_0(\mathbf{r})$ is the ground-state electronic density of the unperturbed system, $V_{[\mathbf{u}]}^{ion}$ is the bare ionic (pseudo) potential acting on the electrons:

$$V_{[\mathbf{u}]}^{ion}(\mathbf{r}) = \sum_{\mathbf{R}_s} v_s(\mathbf{r} - \mathbf{R} - \tau_s - \mathbf{u}_s(\mathbf{R})), \quad (2.28)$$

and $\partial n_{[\mathbf{u}]}(\mathbf{r})/\partial u_{\alpha s}(\mathbf{R})$ is the linear-response of the electron density to the displacement of the s -th ion in the unit cell at \mathbf{R} . The interatomic force constants can be written as a sum of two contributions:

$$C_{\alpha s, \beta s'}(\mathbf{R} - \mathbf{R}') = C_{\alpha s, \beta s'}^{el}(\mathbf{R} - \mathbf{R}') + C_{\alpha s, \beta s'}^{ion}(\mathbf{R} - \mathbf{R}'), \quad (2.29)$$

where the electronic contribution $\mathbf{C}_{ss'}^{el}$ is given by Eq. 2.27, and the ionic one $\mathbf{C}_{ss'}^{ion}$ is the second derivative of the Coulomb interaction between the ionic cores (which is essentially the second derivative of an Ewald sum). The matrix of the interatomic force constants is conveniently calculated in reciprocal space:

$$C_{\alpha s, \beta s'}(\mathbf{R}) = \frac{1}{N} \sum_{\mathbf{q}} \tilde{C}_{\alpha s, \beta s'}(\mathbf{q}) e^{i\mathbf{q}\mathbf{R}}. \quad (2.30)$$

where N is the number of unit cells in the crystal. The electronic contribution is then written in reciprocal space as follows:

$$\begin{aligned} \tilde{C}_{\alpha s, \beta s'}^{el}(\mathbf{q}) &= \int \left[\frac{\partial n(\mathbf{r})}{\partial u_{\alpha s}(\mathbf{q})} \right]^* \frac{\partial V_{ion}(\mathbf{r})}{\partial u_{\beta s'}(\mathbf{q})} d\mathbf{r} \\ &+ \delta_{ss'} \int n_0(\mathbf{r}) \frac{\partial^2 V_{ion}(\mathbf{r})}{\partial u_{\alpha s}(\mathbf{q} = 0) \partial u_{\beta s'}(\mathbf{q} = 0)} d\mathbf{r}, \end{aligned} \quad (2.31)$$

where $\partial V_{ion}(\mathbf{r})/\partial u_{\alpha s}(\mathbf{q})$ is the linear variation of the external ionic potential due to a periodic lattice distortion of wave vector \mathbf{q} :

$$u_{\alpha s}(\mathbf{R}) = u_{\alpha s}(\mathbf{q}) e^{i\mathbf{q}\mathbf{R}}, \quad (2.32)$$

and $\partial n(\mathbf{r})/\partial u_{\alpha s}(\mathbf{q})$ is the corresponding variation of the electron density. Equation 2.31 shows that the harmonic force constants of the crystal can be calculated by first-principles, once the electronic ground-state density of the unperturbed system $n_0(\mathbf{r})$, and its linear response to a lattice distortion of the form 2.32 are known.

When the unperturbed problem is solved in the framework of DFT, the electronic linear response is calculated within Density Functional Perturbation Theory [41, 12] by solving the selfconsistent set of equations:

$$\left[H_{KS} + \tilde{O}_v - \epsilon_i \right] \Delta\psi_i(\mathbf{r}) = -\tilde{P}_c \Delta V_{SCF}(\mathbf{r})\psi_i(\mathbf{r}), \quad (2.33)$$

$$\Delta V_{SCF}(\mathbf{r})\psi_i(\mathbf{r}) = \Delta V_{ion}(\mathbf{r})\psi_i(\mathbf{r}) + 2 \int \frac{\Delta n(\mathbf{r}')}{|\mathbf{r} - \mathbf{r}'|} d\mathbf{r}' + \left. \frac{dv_{xc}}{dn} \right|_{n=n_0(\mathbf{r})} \Delta n(\mathbf{r}), \quad (2.34)$$

$$\Delta n(\mathbf{r}) = 4 \sum_i \psi_i^*(\mathbf{r})\Delta\psi_i(\mathbf{r}), \quad (2.35)$$

where i runs over the occupied states. In the Eqs. 2.33-2.35, in order to simplify the notation, Δf indicates the derivative with respect to the relevant ionic displacements: $\Delta f \equiv \frac{\partial f}{\partial \mathbf{u}}$. $\Delta V_{SCF}(\mathbf{r})$ is the variation of the self-consistent KS potential due to the variation of the *bare* ionic potential produced by the lattice distortion, and it is self-consistently related to the linear variation of the electronic density, $\Delta n(\mathbf{r})$, through the variation of the Hartree and exchange-correlation potentials (Eq. 2.34). The operators \tilde{P}_c and \tilde{O}_v are introduced in order to obtain a numerically stable solution: they orthogonalize the solution with respect to the occupied states and make the system 2.33 non-singular. These two operators are defined in a different way for metallic and non-metallic systems. For non-metallic solids, where empty and occupied states are separated by a finite energy gap, the projection of the perturbed

orbitals over the unoccupied states many-fold is well defined, and it is the solution of Eq. 2.33, where \tilde{P}_c and \tilde{O}_v are defined respectively as:

$$\tilde{P}_c = 1 - \sum_v |\psi_v\rangle\langle\psi_v|, \quad (2.36)$$

$$\tilde{O}_v = \alpha \sum_v |\psi_v\rangle\langle\psi_v|, \quad (2.37)$$

where α is a constant larger than the valence energy band width, in such a way to make the linear system 2.33 non-singular. In this way only the valence states are involved in the computation of the linear variation of the charge density, without explicit introduction of the conduction states. In the case of metals, the smearing technique [42, 43] is used to deal with BZ integration in the presence of a Fermi surface (see the appendix A), so that partially-filled states are introduced. As a consequence, empty and filled states are no more separated in energy, and the projection of $\Delta\psi_i(\mathbf{r})$ over the (partially-) unoccupied states is no longer well defined. In this case the problem is solved by introducing in Eq. 2.33 the “smeared operators” \tilde{P}_c , and \tilde{O}_v , defined as [16]:

$$\tilde{O}_v = \sum_i \alpha_i |\psi_i\rangle\langle\psi_i| \quad (2.38)$$

$$\tilde{P}_c = \tilde{\theta}_{F_i} - \sum_j \beta_{ij} |\psi_j\rangle\langle\psi_j| \quad (2.39)$$

$$\beta_{ij} = \tilde{\theta}_{F_i}\tilde{\theta}_{ij} + \tilde{\theta}_{F_j}\tilde{\theta}_{ji} + \alpha_j \frac{\tilde{\theta}_{F_i} - \tilde{\theta}_{F_j}}{\epsilon_i - \epsilon_j} \tilde{\theta}_{ji} \quad (2.40)$$

where $\tilde{\theta}_{F_i}$ is a smooth approximation of the step function $\theta(\epsilon_F - \epsilon_i)$, α_i being chosen in such a way that the system 2.33 is non-singular, and it is assumed to vanish when ψ_i is unoccupied, so that β_{ij} vanishes when both i and j refer to unoccupied

states. Therefore only the partially filled states enter the definition of these “smeared operators”, and no explicit introduction of the unoccupied states is needed in the computation of $\Delta n(\mathbf{r})$, as for the non-metallic case. A detailed description for practical implementation of force constants calculation within DFPT can be found in reference [12] for insulating systems, and in reference [16] for metals.

Chapter 3

Bulk properties of W

As a preliminary step towards the study of W surfaces, we have studied the structural and lattice-dynamical properties of the bulk metal. The calculations have been performed using plane waves up to a kinetic energy cutoff of 28 Ry (i.e. approximately 300 PW's per atom, at the equilibrium volume) that will be shown to be sufficient to obtain accurate results for the structural and vibrational properties. The Brillouin-zone integration is performed with the “smearing” technique of reference [43], using the Hermite-Gauss smearing function of order $N = 1$ (see appendix A) and a smearing width $\sigma = 70$ milliRydbergs (mRy). Accurate checks have shown that this width results in a satisfactory convergence of the calculated quantities. The BZ sampling is performed on a uniform cubic grid in \mathbf{k} -space, following the Monkhorst and Pack scheme [44]. Using the point symmetry of the lattice, only points in the so called irreducible wedge (IW) need to be sampled. The smaller the value of σ , the finer is the mesh needed to achieve convergence with respect to the number of sampling \mathbf{k} -points. For $\sigma = 70$ mRy a mesh of 55 points in the

IW is enough. We use the *ab initio* norm-conserving pseudopotential of Bachelet, Hamann, and Schlüter [31] in the separable KB form [36], with non locality in the angular momentum up to $l_{\max} = 2$, and $l^* = 1$ for the reference local potential. For the local exchange-correlation energy we choose the parameterization of Perdew and Zunger [45]. The vibrational properties are studied using *ab initio* interatomic force constants calculated within the Density-Functional Perturbation Theory [12, 16, 41].

3.1 Equilibrium structure

Tungsten is a transition metal that crystallizes in the monoatomic bcc lattice. The equilibrium structure is determined by minimizing the total energy of the crystal with respect to the lattice parameter. For this purpose, the values of the total energy calculated with a fixed kinetic-energy cutoff at different lattice parameters, a , have been fitted to a Murnaghan's equation of state:

$$E(\Omega) = \frac{\Omega_0 B_0}{B'_0} \left[\frac{1}{B'_0 - 1} \left(\frac{\Omega_0}{\Omega} \right)^{B'_0 - 1} + \frac{\Omega}{\Omega_0} \right] + \text{const}, \quad (3.1)$$

where B_0 is the bulk modulus, B'_0 its derivative with respect to the pressure, and $\Omega_0 = a_0^3/2$ the equilibrium volume of the unit cell. Figure 3.1 shows the calculated energies and the corresponding Murnaghan's fit, for different cutoffs between 20 and 32 Ry. The results of the interpolations are collected in Table 3.1. A cutoff of 28 Ry is enough to obtain a convergence for the structural parameters within 1%, and of the order of the mRy for the total energy. The discrepancy with the experimental values is 1% for the lattice parameter and 7% for the bulk modulus. This agreement is good and comparable with the typical accuracy of LDA calculations for semiconductors

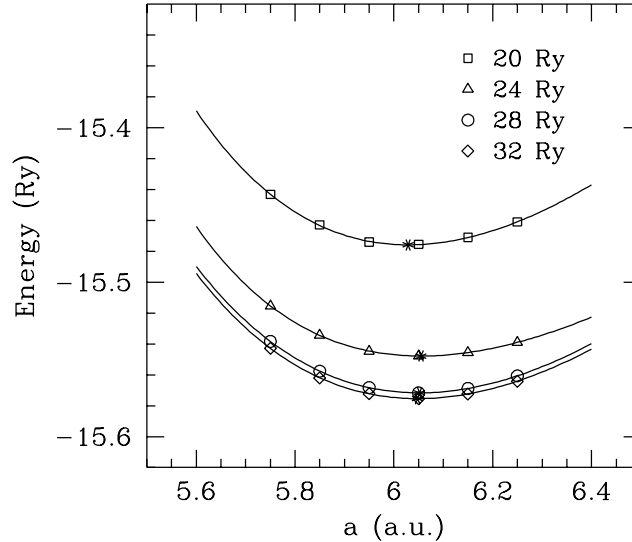


Figure 3.1: Total energy of bulk Tungsten vs lattice parameter, for different energy cutoffs. The open symbols indicate calculated values. The stars correspond to the minimum energy. Least-squares fit with Murnaghan's equation of state are shown with solid lines.

and other metals. Convergence with respect BZ sampling and smearing width, σ , has been further checked, finding only a slight dependence of the structural parameters upon the value of σ . A more critical behaviour is shown instead by the phonon frequencies (see next Section). The value for σ has therefore been fixed by requiring good convergence on the frequencies. As explained in Sect. 2.1.2, a suitable choice of the reference local potential can eliminate possible ghost states that may occur when the pseudopotential is used in the KB form. We have found that with the usual choice $l^* = l_{\max}$ for the reference local potential, two ghosts appear in the s and p spectrum of the isolated atom at low energy. We have obtained a *ghost-free* pseudopotential using $l^* = 1$. The choice of l^* would not be critical if one did not adopt the KB representation of the pseudopotential. As a check we have compared

Table 3.1: Convergence study with respect to the energy cutoff for structural parameters of W bulk. Experimental data are reported as comparison.

	20 Ry	24 Ry	28 Ry	32 Ry	Exp. [46]
a_0 (a.u.)	6.03	6.06	6.05	6.05	5.97
B_0 (GPa)	378	291	334	333	311
B'_0	4.8	5.7	4.1	4.3	–

our results to those obtained using the SL form for the pseudopotential with the different choices of l^* , we find no substantial differences: the use of $l^* = 1$ instead of $l^* = 2$ gives larger values of 2% for a_0 , and of 10% for B_0 and B'_0 .

3.2 Dynamical properties

Transition metals are known to present anomalies in the phonon dispersions [47, 48, 49] due to singularities in the electronic screening that can occur when the periodicity of the involved lattice distortion connects different portions of the Fermi surface [50]. When almost parallel portions of the FS are *nested* by a wave vector $\mathbf{q}_c = 2\mathbf{k}_F$ (where \mathbf{k}_F is a vector on the Fermi surface) a relatively large number of states \mathbf{k} and $\mathbf{k} + \mathbf{q}_c$ with small energy difference is available around the Fermi level. This may give rise to a strong enhancement of the electronic screening in correspondence to the wave vector \mathbf{q}_c that results in a reduction of the screened ion-ion interactions and of the corresponding phonon frequency. As a consequence so called *Kohn anomalies* appear in the phonon dispersions, as kinks or softenings, at the nesting wave vectors \mathbf{q}_c . For example in the phonon dispersions of bulk W

a clear dip occurs at the H-point of the BZ, because the dielectric susceptibility is enhanced near the H point by the nesting properties of the Fermi surface [49].

The smearing technique, used to deal with \mathbf{k} -space integration, introduces a broadening in the occupation of the electronic states near the Fermi level, whose effect is similar to that of a fictitious finite electronic temperature ($\sigma \sim T$). Since the Kohn anomalies are strictly related to the sharpness of the Fermi surface, they depend quite sensitively upon temperature. Therefore we have performed accurate test calculations in two representative points of the BZ, the anomalous H point and the regular P point, using different values for σ between 5 and 70 mRy. Different sampling meshes up to 728 \mathbf{k} -points in the IW have been used in order to ensure that the results were adequately converged with respect to the BZ sampling. Both modes $\omega(\text{H})$ and $\omega(\text{P})$ are threefold degenerate by symmetry, and are found experimentally to have practically the same frequency $\approx 183 \text{ cm}^{-1}$. An extrapolation of our calculations to zero smearing width gives the converged value, 187 cm^{-1} for both frequencies, with an agreement of 3% with the experiment. As expected the anomalous frequency $\omega(\text{H})$ has a stronger dependence on σ than $\omega(\text{P})$, that is already converged within 1% for $\sigma = 70 \text{ mRy}$. In order to have the same accuracy for $\omega(\text{H})$ a smaller value $\sigma=5 \text{ mRy}$ and 728 \mathbf{k} -points should be used. Phonon dispersions were calculated throughout the BZ using the smearing width $\sigma = 70 \text{ mRy}$ and 55 points in the IW. Convergence with respect to the energy cutoff has been also checked. An energy cutoff of 28 Ry is sufficient to obtain frequencies converged within $1 \div 2\%$.

3.2.1 Real-space interatomic force constants

The force constants $\mathbf{C}(\mathbf{R})$ become negligible for interatomic distances \mathbf{R} sufficiently large. The finite number of relevant non vanishing real-space interatomic force constants can be therefore calculated by Fourier analyzing their reciprocal-space counterpart, Eq. 2.30, computed on a discrete mesh. The larger the number of real-space force constants one wants to calculate, the finer must be the reciprocal-space mesh. In order to obtain the force constants up to an interatomic distance R_{\max} the discretization parameter of the reciprocal space grid should be $\Delta q \sim \frac{2\pi}{R_{\max}}$. We used a grid defined by the \mathbf{q} points:

$$\mathbf{q}_{lmn} = \left(\frac{l}{L}, \frac{m}{L}, \frac{n}{L} \right) \frac{4\pi}{a} \quad 0 \leq l \leq L-1, \quad 0 \leq m \leq L-1, \quad 0 \leq n \leq L-1, \quad (3.2)$$

which corresponds to a uniform mesh in the cube that contains the bcc BZ. In particular we have calculated the force-constant matrices at all the \mathbf{q} points corresponding to $L = 8$. Calculations have been done explicitly for the \mathbf{q} points within the IW (i.e. 14 points); the force constants at all the other \mathbf{q} points are obtained by symmetry. In this way we are accounting for the interactions between each atom and all those which lie in a cube of edge $4a$ centered at its position. Once real-space force constants have been obtained in this way, reciprocal space dynamical matrices can be calculated by inverse Fourier transform, Eq. 2.24, at any point of the BZ.

3.2.2 Phonon dispersions

Our phonon dispersions for W, calculated along several symmetry lines, are displayed in Fig. 3.2; experimental data from neutron scattering experiment [51] are denoted by diamonds. All the anomalous features found experimentally are well reproduced:

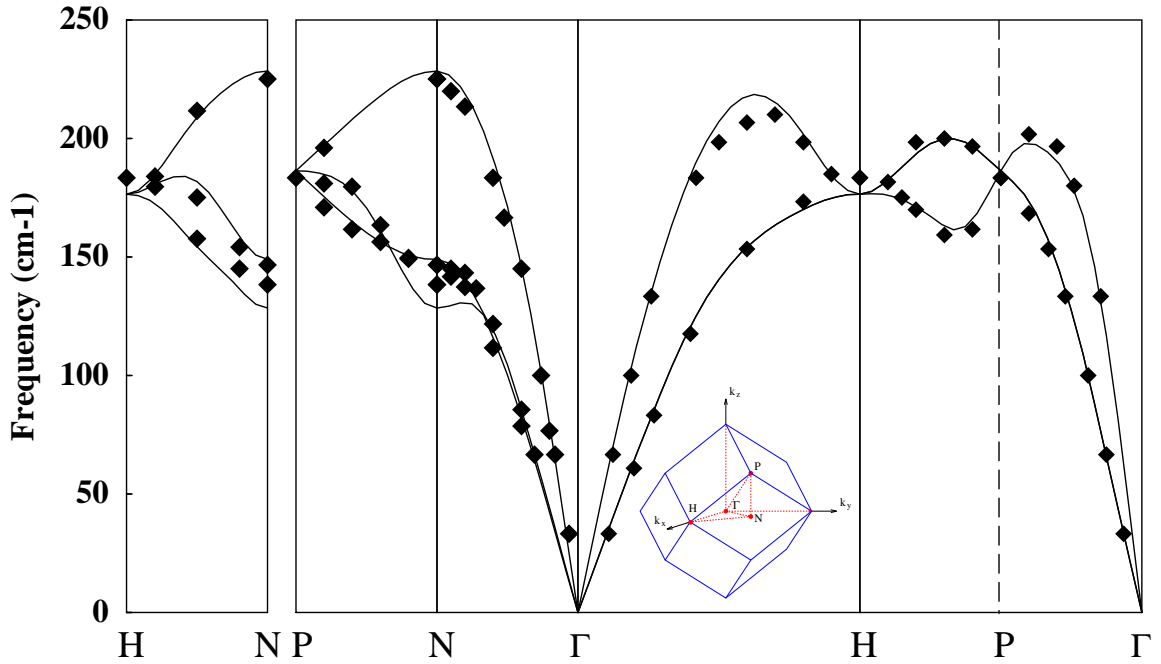


Figure 3.2: Phonon dispersions for bulk W: our calculations are shown by solid lines and the neutron scattering data from Ref.[51] are denoted by diamonds. The bcc BZ is shown in the inset.

the softening of the longitudinal branch at the H point; the dip in the longitudinal branch along the H-P direction; the crossing of the two transverse branches along Γ -N due to the steep decrease of one of them near N. The overall agreement is within the typical accuracy of DFPT calculations of about 1%, except near the anomalies, where a worse accuracy of about 6% should have been expected on the basis of the previous convergence study.

Chapter 4

Clean and hydrogenated W(110) surfaces

In this chapter we present the results of our study of clean and hydrogenated (110) surfaces of Tungsten. The hydrogenated surface, H/W(110), is covered by a full monolayer of hydrogen, i.e. the coverage at which the surface phonon anomalies have been observed experimentally. The surface properties are studied by modeling the W(110) surface with a slab of 7 atomic layers of Tungsten. In order to introduce a three-dimensional periodicity, we have used the “supercell geometry”, by repeating the W slabs in the [110] direction. A vacuum region of 20.5 Å (equivalent to 8 layers of W) separates one slab from the other. The full Coulomb $1/r$ potential is used for hydrogen. We have performed the BZ integration using a mesh of 16 **k** points [52] in the IW of the two-dimensional surface Brillouin zone (SBZ). This grid has approximately the same density in the [110] plane as the grid of 55 **k**-points used for bulk calculations. Since the anomalous phonon frequencies of the hydrogenated

surface are thought to have an important dependence upon the nesting features of the Fermi surface, we expect these modes to have a critical dependence upon the smearing width σ . We have studied accurately this issue using smaller value of σ down to 2.5 mRy and accordingly finer SBZ sampling up to 324 \mathbf{k} points in the IW.

4.1 Equilibrium structures

It is well known that the equilibrium atomic positions in a crystal surface are generally different from those in the ideal bulk-terminated surface (i.e. a surface simply obtained by cutting the infinite perfect crystal along a plane of bonds and leaving the interatomic distances unchanged).

As a first step we have determined the equilibrium atomic geometry of the W(110) and H/W(110) surfaces. To this purpose we minimize the total energy as a function of the atomic positions in order to find the zero-force atomic configuration. The minimization is performed with the help of Hellmann-Feynman forces and following the Broyden-Fletcher-Goldfarb-Shanno algorithm [53].

It is well established, from different experimental analysis, that the clean surface is unreconstructed [54]. The surface retains the same centered rectangular structure of a bulk (110) layer, as shown Fig. 4.1. In our supercell we have one W atom per layer. The equilibrium atomic configuration of the unreconstructed W(110) surface is found by minimizing the total energy with respect to the intralayer distances d_{ij} indicated in the side view of Fig. 4.1. Our results for the relaxation parameters $\Delta d_{ij} = (d_{ij} - d_0)/d_0$ are collected in Table 4.1, where $d_0=2.27 \text{ \AA}$ is the unrelaxed intralayer distance in the bulk. We find a small inward relaxation of -2.9% in the

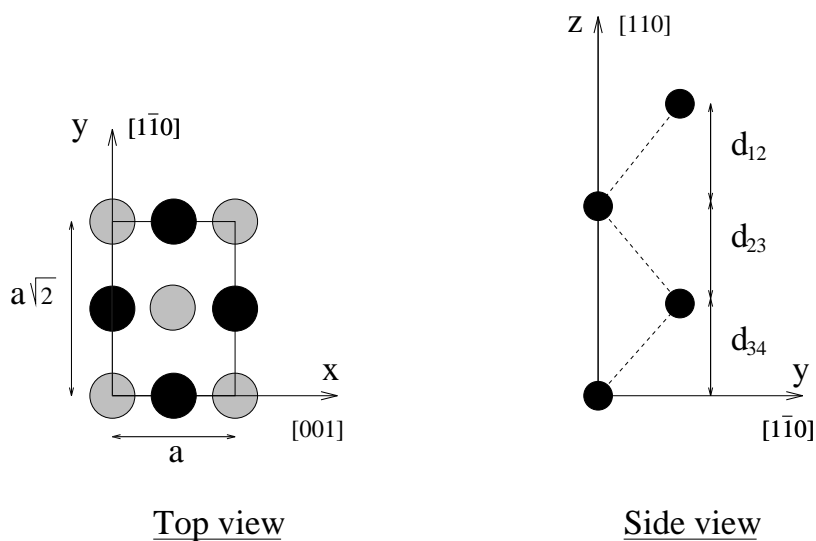


Figure 4.1: Surface geometry of W(110). The z direction is perpendicular to the surface. Left: a top view with first-layer W atoms in black and second-layer ones shaded. Right: a side view, only one W atom per layer is indicated (black full circles). a is the bulk lattice parameter of W.

first intralayer spacing. The other interplanar distances are substantially unchanged, considering that the numerical accuracy is of the order of $\pm 0.1\%$.

In order to determine which is the most stable adsorption site for hydrogen, we have calculated the energy adsorption differences ΔE_{ad} for the most important sites indicated in the top view of Fig. 4.2. For each hydrogen position we have relaxed the atomic coordinates in our supercell. The calculated adsorption energies are summarized in Table 4.1 together with the corresponding relaxation parameters. The hollow site results to be the most favorable in agreement with EELS measurements [21]. Both short- and long-bridge positions are clearly energetically unfavorable, and the on-top position is even worse. The inward relaxation of the first intralayer distance, d_{12} , is reduced when hydrogen is adsorbed in the hollow,

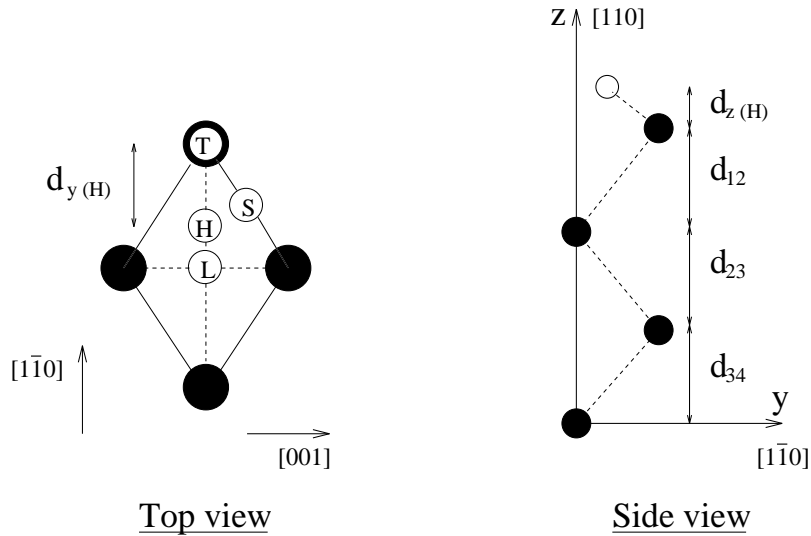


Figure 4.2: Surface geometry of the H/W(110) surface. The z direction is perpendicular to the surface. Left: a top view with first-layer W atoms in black. The different H sites long-bridge (L), short-bridge (S), hollow (H), and on-top (T) are also indicated. Right: a side view; only one W atom per layer is indicated (black full circles) and the smaller white circle on top of the surface indicates the hydrogen atom.

short-bridge, and long-bridge sites. For on-top adsorption an outward relaxation is observed. In Table 4.1 we also report the height $d_{z(H)}$ of the H atom above the surface obtained for the different adsorption sites, and its $[1\bar{1}0]$ offset $d_{y(H)}$ from the on-top position when adsorbed in the hollow site (see Fig. 4.2). Estrup et al. have found a loss of symmetry in their LEED spectra when the W(110) surface is covered by more than half monolayer of hydrogen, and proposed that a displacement of the top layer of W atoms would occur along the $[1\bar{1}0]$ direction [20]. With the hydrogen in the hollow position we find a small shift, $\Delta y_1 = -0.05 \text{ \AA}$, of the first W layer along this direction. According to these findings, we will assume hereafter the

hydrogen atoms stay at their most stable hollow position. Similar results for the relaxed structures of the clean and hydrogenated surfaces have also been obtained previously using the full-potential linearized augmented plane wave method [25].

Table 4.1: Calculated relaxation parameters and adsorption energy differences for the clean and hydrogenated W(110) surfaces. Results for hydrogen adsorbed in the hollow, long-bridge, short-bridge, and on-top sites are compared. $d_{z(H)}$ is the height of the hydrogen above the surface, and $d_{y(H)}$ its $[1\bar{1}0]$ offset from the on-top position. Δd_{ij} indicates the change of the intralayer distance between the i -th and the j -th layer with respect to the bulk interplanar spacing, d_0 . Δy_1 is the shift of the topmost W layer with respect to the substrate, along the $[1\bar{1}0]$ direction.

	clean	hydrogenated			
		hollow	short bridge	long bridge	on top
$d_{z(H)}$ (Å)	–	1.15	1.38	1.15	1.80
$d_{y(H)}$ (Å)	–	1.62	–	–	–
Δd_{12} (% d_0)	–2.9	–1.5	–1.2	–0.8	+1.6
Δd_{23} (% d_0)	+0.3	–0.1	–0.1	–0.3	–0.9
Δd_{34} (% d_0)	–0.1	–0.2	–0.2	–0.2	–0.2
Δy_1 (Å)	–	–0.05	–	–	–
ΔE_{ad} (eV)	–	0	0.11	0.32	0.96

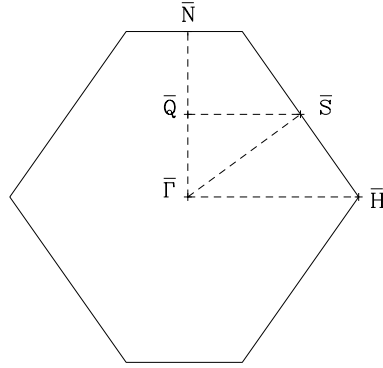


Figure 4.3: Two-dimensional surface Brillouin zone (SBZ). Points along symmetry lines are marked. The coordinates of high symmetry points in $2\pi/a$ unit are: $\bar{H}=(3/4,0)$, $\bar{N}=(0,\sqrt{2}/2)$, $\bar{S}=(1/2,\sqrt{2}/4)$.

4.2 Electronic properties

Metals in low dimensions are often characterized by an enhanced nesting of their Fermi surface, so that strong Kohn anomalies are expected to occur [55]. Giant Kohn anomalies have been observed in certain systems of effectively reduced dimensionality, such as layer and chain bulk compounds [56, 7], due to the presence of extended almost parallel portions of the Fermi surface.

Since the electronic properties at the Fermi level play such an important role in the vibrational properties, we have calculated the band structure and the Fermi surfaces for the clean and H-covered W(110) surfaces, and analyzed their nesting properties. The slab band structure of the clean and hydrogenated W(110) surfaces, along the $\bar{\Gamma}\bar{S}$ and $\bar{Q}\bar{S}$ lines in the SBZ (shown in Fig. 4.3) are reported in Fig. 4.4. The energies from bulk and slab calculations are aligned by matching the corresponding Fermi levels. The slab states within the gap of the surface-projected bulk bands (i.e. within the energy regions forbidden in the bulk), are surface states. The

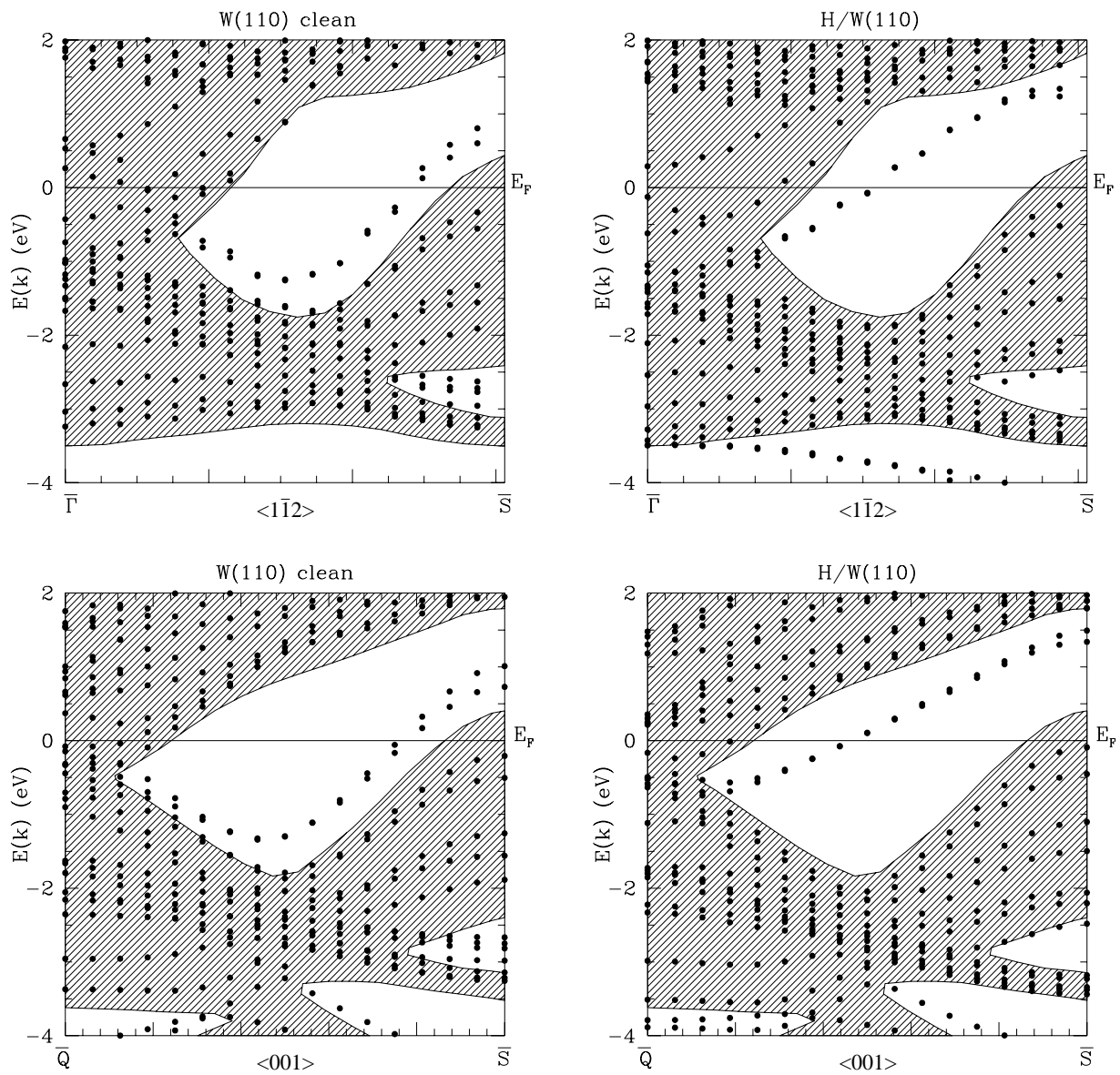


Figure 4.4: Surface band structure of clean and H-covered W(110) surfaces from a 7 W-layers slab calculation (full dots), along the $\overline{\Gamma}\overline{S}$ and $\overline{Q}\overline{S}$ lines in the SBZ. Shaded areas are the surface-projected band structure of the bulk. The zero of the energy corresponds to the Fermi level.

corresponding wave functions have their maximum amplitude near the surface and decay exponentially into the slab. Since the calculations are performed using the slab geometry, all surface states occur pairwise, one from each surface of the slab. Due to the finite thickness of the slab, states localized on the two surfaces can couple, and the degeneracy may be lifted. The stronger the surface character of the states, the smaller is the splitting between the two levels.

In the band structure of the clean W(110) surface (left panels in Fig. 4.4), a surface state is present along the $\overline{\Gamma S}$ and the \overline{QS} lines, which intersects the Fermi level. This state is quite close to the bulk energies and it is not very localized at the surface, as can be seen from the rather large splitting. When a full monolayer of hydrogen is adsorbed on the surface (right panels in Fig. 4.4), this state is pushed towards higher energy in the middle of the gap of bulk states, and its surface character is enhanced: the pair of states corresponding to the two surfaces of the slab are in fact almost perfectly degenerate in the H-covered surface. We are particularly interested in what happens at the Fermi level. In figure 4.5 we show the Fermi surfaces calculated for the clean W(110) and the hydrogenated H/W(110) surfaces. The shaded region is the projection of the bulk Fermi surface on the SBZ. The solid lines that fall outside the shaded region, indicate the FS of the surface states previously discussed: they form a circuit of elliptical shape around the \overline{S} point, and are hole orbits in the sense that enclose unoccupied levels. The effect of hydrogen adsorption is to enlarge the contours of the surface-localized Fermi surface, pushing it well inside the bulk gap. The existence of these elliptically shaped portions of the surface Fermi surfaces around the \overline{S} point has been also found experimentally with high-resolution angle-

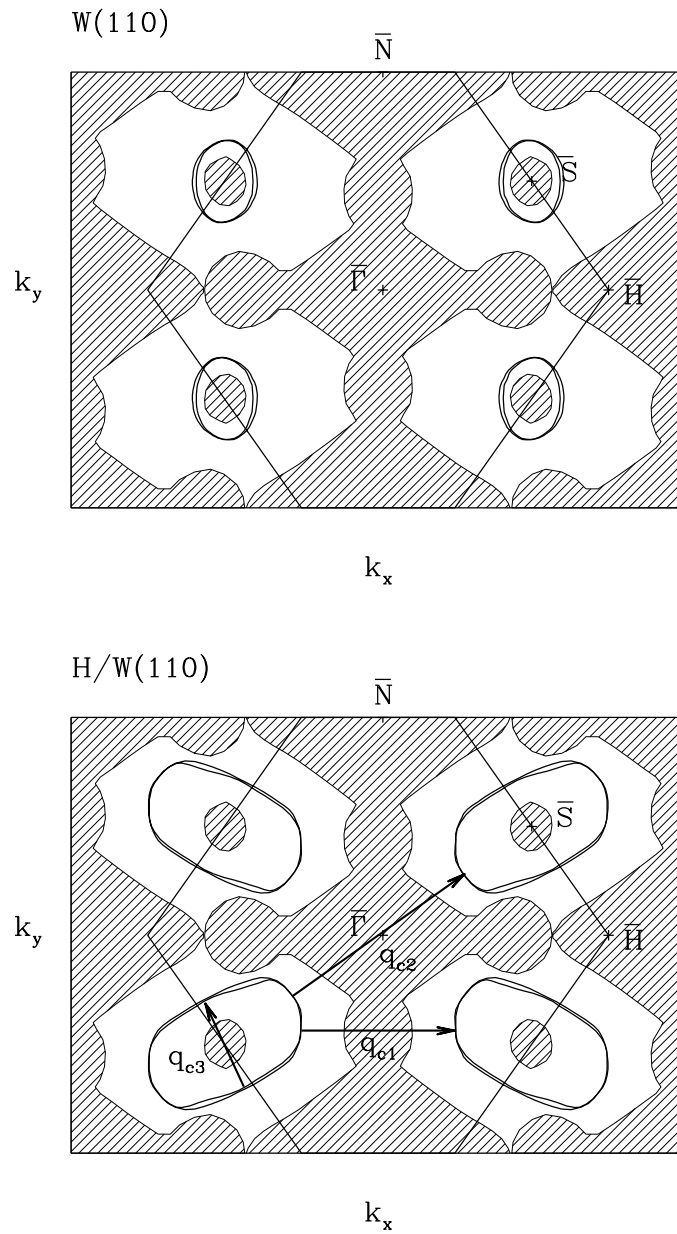


Figure 4.5: Calculated Fermi surfaces of the surface-localized states (solid lines), for the clean (upper panel) and H-covered (lower panel) W(110) surfaces. The shaded region is the projection of calculated FS of the bulk, within the SBZ. \mathbf{q}_{c1} , \mathbf{q}_{c2} and \mathbf{q}_{c3} indicate the nesting vectors for the hydrogenated surface. The contour of the SBZ, and the high symmetry points are also indicated.

Table 4.2: Theoretical Fermi surface nesting wave vectors compared to the critical wave vector of phonon anomalies measured in HAS and EELS experiments. The results are reported both in \AA^{-1} and in units of $\frac{2\pi}{a}$, where a is the lattice parameter.

		q-direction	Theory	Exp. ^{a,b}
\mathbf{q}_{c1}	(\AA^{-1})	$\overline{\Gamma\text{H}}$	0.88	0.95
	$(\frac{2\pi}{a} \text{ units})$		(0.45)	(0.48)
\mathbf{q}_{c2}	(\AA^{-1})	$\overline{\Gamma\text{S}}$	1.21	1.22
	$(\frac{2\pi}{a} \text{ units})$		(0.62)	(0.61)
a	(\AA)		3.20	3.16

^aRef. [3], ^bRef. [6]

resolved photo emission-measurements [9] (ARP). In agreement with our findings the experimental data also indicate that these elliptical orbits are enlarged when the hydrogen is adsorbed on the surface, but their shape differs considerably from the theoretical one (see Fig. 4.6).

The theoretical Fermi surface of the hydrogenated surface presents parallel portions associated with well localized surface states, that give rise to a quasi one-dimensional nesting. The wave vectors connecting these states are \mathbf{q}_{c1} , parallel to the $\overline{\Gamma\text{H}}$ direction, and \mathbf{q}_{c2} , parallel to the $\overline{\Gamma\text{S}}$ direction. These nestings can give rise to pronounced Kohn anomalies in the phonon dispersions in correspondence of the critical wave vectors \mathbf{q}_{c1} and \mathbf{q}_{c2} . In Table 4.2 the nesting wave vectors which result from our calculations are compared with the critical wave vectors at which the phonon anomalies have been detected by HAS and EELS experiments [3, 6]:

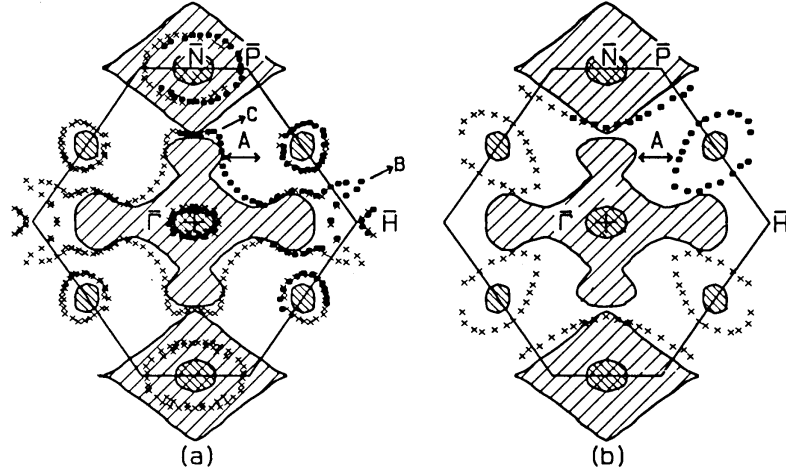


Figure 4.6: Experimental Fermi surface contours for (a) the clean W(110) and (b) the H/W(110) surfaces from ARP measurements of Ref.[9].

resulting in very good agreement. Similar results have also been obtained by a previous calculation [25]. Since the states connected by the nesting are well-localized surface states, one expects the surface phonon modes that are well localized at the surface to be mostly affected by the corresponding Kohn anomaly. Contrary to these theoretical results, the experimental Fermi surfaces (see Fig. 4.6) do not provide any evidence of nesting vectors in correspondence of the detected anomalies. The disagreement between the experimental and the theoretical FS contours may be attributed to the approximations used in the calculations or to some lack of accuracy in the experiments. The theoretical Fermi surfaces have been obtained within LDA and neglecting e-ph interactions (adiabatic approximation). The nesting features revealed by the FS calculated under these assumptions indicate that the e-ph

coupling is strongly enhanced at the nesting wave vectors, thus possibly modifying the profile of the Fermi surfaces expected from experiments which obviously probe dressed rather than bare quasiparticle excitations. In any case the nesting mechanism that is at the origin of the Kohn anomalies arises from features of the adiabatic Fermi surface. Therefore the absence of nesting features in the experimental FS is not compelling. Moreover we note that the Fermi surface reported in Ref. [9] is affected by some inconsistency as regards its symmetry properties. In fact the elliptical orbits centered at \bar{S} should coincide with that centered at $-\bar{S}$ when translated by the reciprocal lattice vector $\mathbf{G} = (1, \sqrt{2}/2)2\pi/a$. As this is not clearly the case in Fig. 4.6, we cannot rule out that this is due to some inaccuracy in the experimental data.

We suggest the presence of a third nesting wave vector \mathbf{q}_{c3} that can give rise to a corresponding Kohn anomaly. This wave vector connects states which have a weaker surface character than the states connected by the nesting vectors \mathbf{q}_{c1} and \mathbf{q}_{c2} . We expect that its effective coupling with surface phonons and the related Kohn anomaly are therefore less pronounced.

4.2.1 Work function

The work function \mathcal{W} is defined as the minimum energy required to extract one electron from the metal. We have computed the work function, for the clean and the hydrogenated W(110) surfaces, as $\mathcal{W} = V_0 - E_F$, where E_F is the Fermi energy and V_0 is the value of the electrostatic potential energy in the middle of the void region of our supercell, which mimics the vacuum. The planar and macroscopic

Table 4.3: Computed values of the work function W_{clean} for the clean W(110) surface and of its change upon hydrogenation. Experimental data are reported for comparison.

	Theory (eV)	Experiment (eV)
W_{clean}	5.22	5.25 ^a
$(W_{\text{clean}} - W_{\text{H-covered}})$	0.54	0.48 ^b

^aRef. [59], ^bRef. [58]

averages (see Ref. [57]) of the electrostatic energy for the clean and hydrogenated surfaces are shown in the Figs. 4.7 and 4.8, together with the planar and macroscopic averages of the electronic density.

The calculated work function W_{clean} for the clean surface is in remarkable agreement with the experimental value. Experimental measurements [58] have shown that the work function of the hydrogenated W(110) surface decreases monotonically with increasing hydrogen coverage up to a full monolayer. In good agreement with the experiment we find that at a full hydrogen coverage the work function is reduced by ≈ 0.5 eV (see Table 4.3).

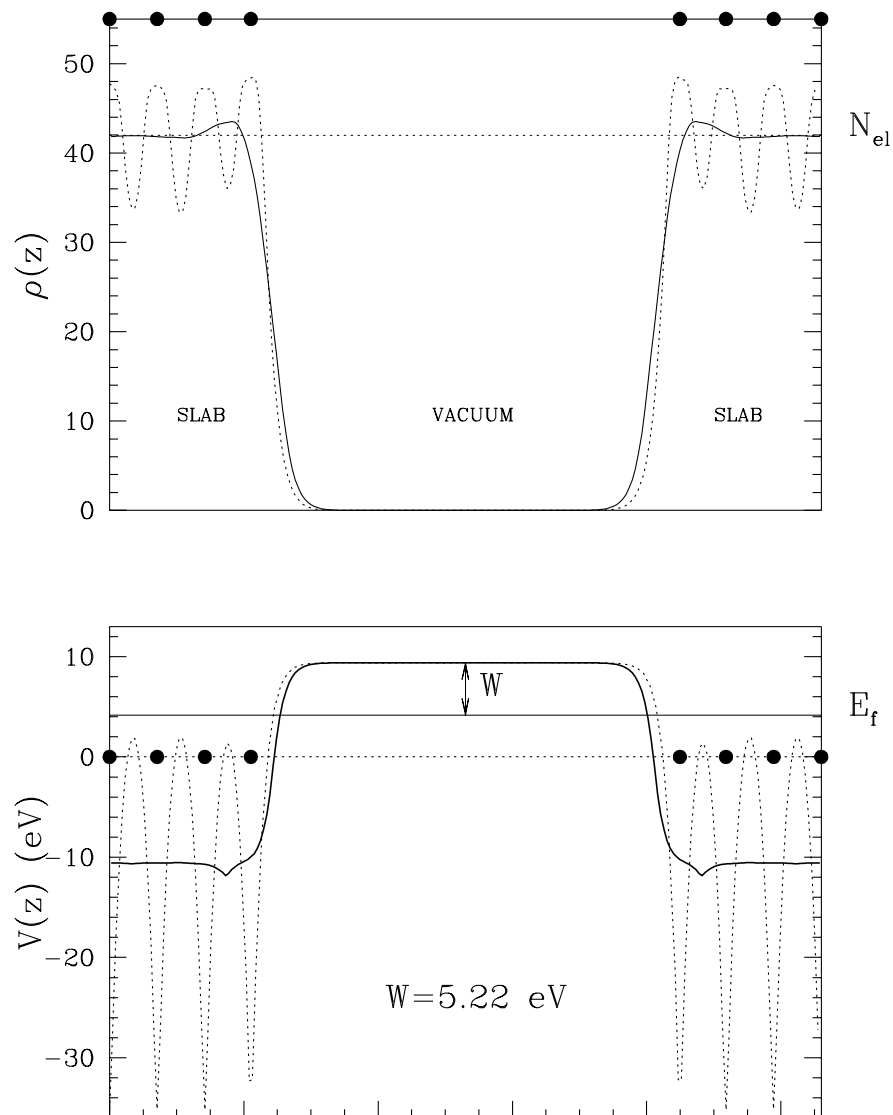


Figure 4.7: Planar and macroscopic averages (dotted and solid line) of the electronic density (upper panel) and electrostatic energy (lower panel) for the W(110) surface. z is the direction perpendicular to the surface. The full dots indicate the position of W atoms within the slab. The work function W is also reported.

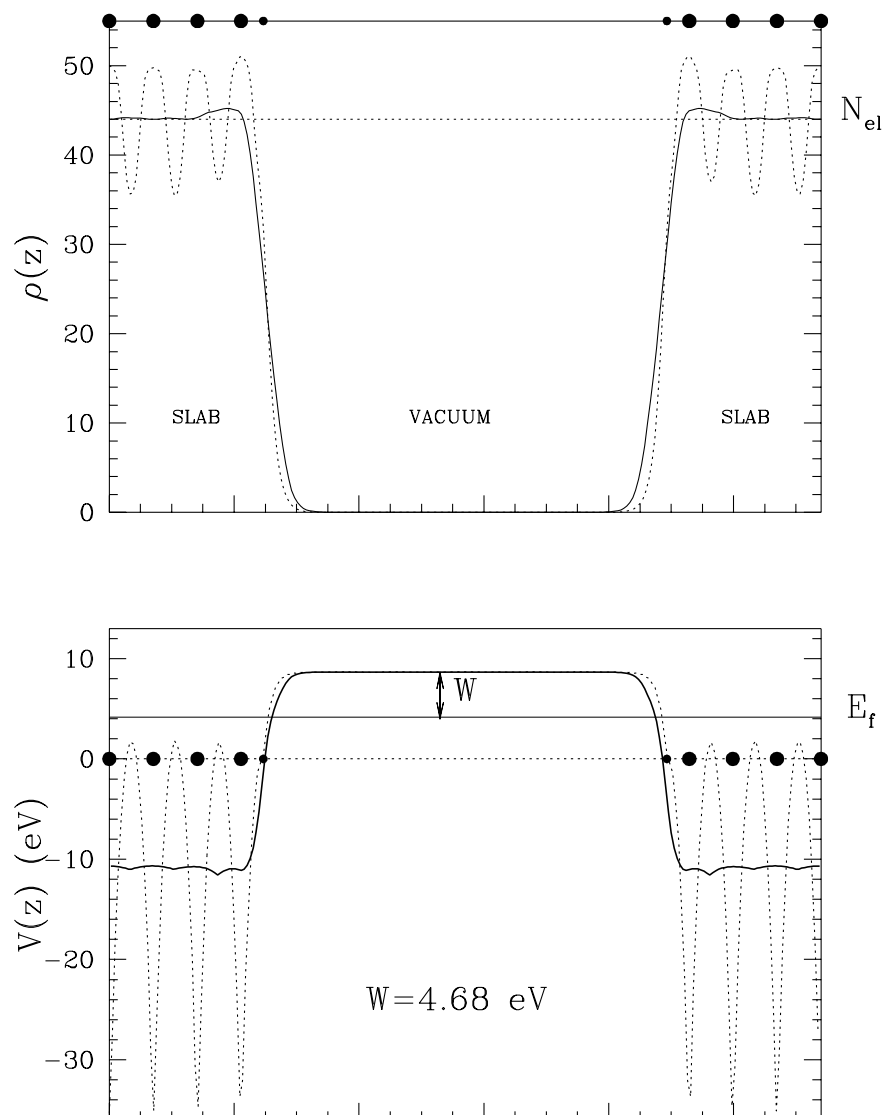


Figure 4.8: Planar and macroscopic averages (dotted and solid line) of the electronic density (upper panel) and electrostatic energy (lower panel) for the H/W(110) surface. z is the direction perpendicular to the surface. The big full dots indicate the position of W atoms within the slab, the small one is the H atom. The work function \mathcal{W} is also reported.

4.3 Vibrational properties

The surface lattice dynamics has been dealt with by calculating the harmonic force constants of the fully relaxed slab of seven W-layers (plus the two H-layers in the case of the H-covered surface). We have verified that the force constants coupling atoms on the opposite surfaces of the slab are negligible, and that those which couple the central layer to the other ones are very close to the force constants calculated for the bulk. This guarantees that the two surfaces of the slab are decoupled and that the surface force constants are well described. A thicker slab is necessary to decouple the surface vibrational modes which penetrate more than three layers. Therefore the force constants calculated for the 7-layer slab were used to model the dynamical matrices of a much thicker slab builded up by inserting a number of bulk layers in the middle of the seven-layer slab, as sketched in Fig. 4.9. The force constants between atoms in the four surface layers of such a thicker slab (S blocks in Fig. 4.9), are those calculated for the seven-layer slab:

$$\mathbf{C}_{ss'}(\mathbf{q}_{\parallel}) = \mathbf{C}_{ss'}^{7\text{-layer}}(\mathbf{q}_{\parallel}), \quad (4.1)$$

where s , and s' correspond to the atoms on the four topmost layer of the slab surfaces. All the other force constants are taken equal to the interatomic force constants in the bulk, $\mathbf{C}^{\text{bulk}}(\mathbf{R})$, previously calculated (see Sect. 3.2.1). Therefore, for any wave vector \mathbf{q}_{\parallel} in the SBZ, the force constants “shaded” in Fig. 4.9 (describing the bulk-bulk and bulk-surface interactions) have been obtained as follows:

$$\mathbf{C}_{ss'}(\mathbf{q}_{\parallel}) = \sum_{\mathbf{R}_{\parallel}} \mathbf{C}^{\text{bulk}}(\mathbf{R}_s - \mathbf{R}'_s) e^{-i\mathbf{q}_{\parallel}(\mathbf{R}_s - \mathbf{R}'_s)}, \quad (4.2)$$

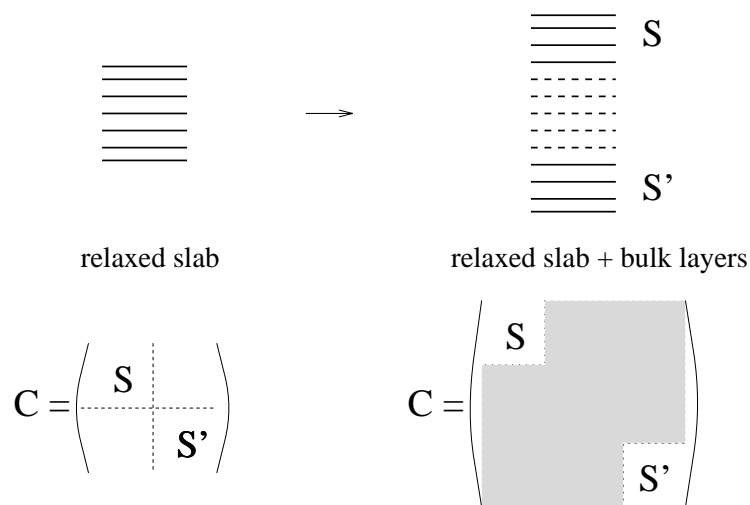


Figure 4.9: Sketch of the procedure used to model the force constant matrix C of a thick slab (on the right). The force constants calculated for a seven-layer relaxed slab (S blocks) describe the interactions between atoms in the four topmost surface layers (solid lines) of the thick slab. Dashed lines indicate bulk layers inserted in order to make the slab thicker. The force constants describing bulk-bulk and bulk-surface interactions are indicated by the shaded blocks, and have been assumed to be equal to the interatomic force constants of the bulk.

where \mathbf{R}_{\parallel} runs over the two-dimensional direct lattice of the surface, and $\mathbf{R}_s = \mathbf{R}_{\parallel} + \tau_s$.

The normal modes of the slab can be classified [60] as surface modes, bulk modes, or resonances according to the behaviour of the atomic-displacement amplitudes as the center of the slab is approached, and provided that the slab is sufficiently thick. For \mathbf{q} points along high symmetry directions in the two-dimensional surface Brillouin zone, the normal modes can be further classified according to their symmetry. Modes in which the atomic displacements lie in the sagittal plane defined by the normal to the surface and the direction of \mathbf{q} (which is parallel to the surface) are referred to as sagittal modes. Modes in which the displacements are normal to the sagittal plane, are referred to as shear horizontal (SH) modes. Selection rules allows both helium atom scattering and electron energy loss spectroscopy to sample only modes with displacements in the sagittal plane.¹

¹This is true in the usual experimental configuration for which the scattering plane is a reflection plane. The SH modes can be measured by tilting the sample in such a way that the scattering plane does not contain the surface normal [61].

4.3.1 Clean surface

The phonon dispersions of the clean W(110) surface, calculated along the $\overline{\Gamma\text{H}\overline{\text{N}}}$ line² using a slab of 69 W-layers, are shown with green lines in Fig. 4.10. The branches that fall outside the region of bulk projected modes, which is delimited by the thick blue lines, are surface modes. The surface modes do not change significantly for slabs thicker than 15 layers. The only important effect of increasing further the slab thickness is to provide more dense mode frequencies in the bulk region. We have checked that the calculated frequencies are converged within about 1% with respect to the broadening width using $\sigma=70$ mRy.

The surface phonon dispersions of the W(110) surface have been measured both by HAS [2, 3] and EELS [6] experiments. The intensity of the He inelastic scattering decreases towards the SBZ boundary, along $\overline{\Gamma\text{H}}$. Therefore the dispersion curves have only been measured for wave vectors within the first two thirds of the SBZ. The EELS measurements have detected the whole dispersion up to the SBZ boundary, and are in excellent agreement with the HAS data where available. Therefore we compare our calculation with the more complete EELS data which are indicated with the red dots in Fig. 4.10, and we find a remarkably good agreement.

In order to evidenciate which ones of the calculated slab modes have a dominant surface character, and how these modes are polarized, we have calculated their localization rate, defined as:

$$l_\alpha(\nu, \mathbf{q}) = \frac{\sum_n u_{\alpha n}^2(\nu, \mathbf{q})}{\|\mathbf{u}(\nu, \mathbf{q})\|^2}, \quad \text{with } \alpha = x, y, z \quad (4.3)$$

where $\mathbf{u}(\nu, \mathbf{q})$ is the amplitude of the atomic displacements for the ν -th normal mode

²i.e. for wave vectors $\mathbf{q} = (q_x, 0)$, at the point $\overline{\text{N}}$ is $q_x = 2\pi/a$.

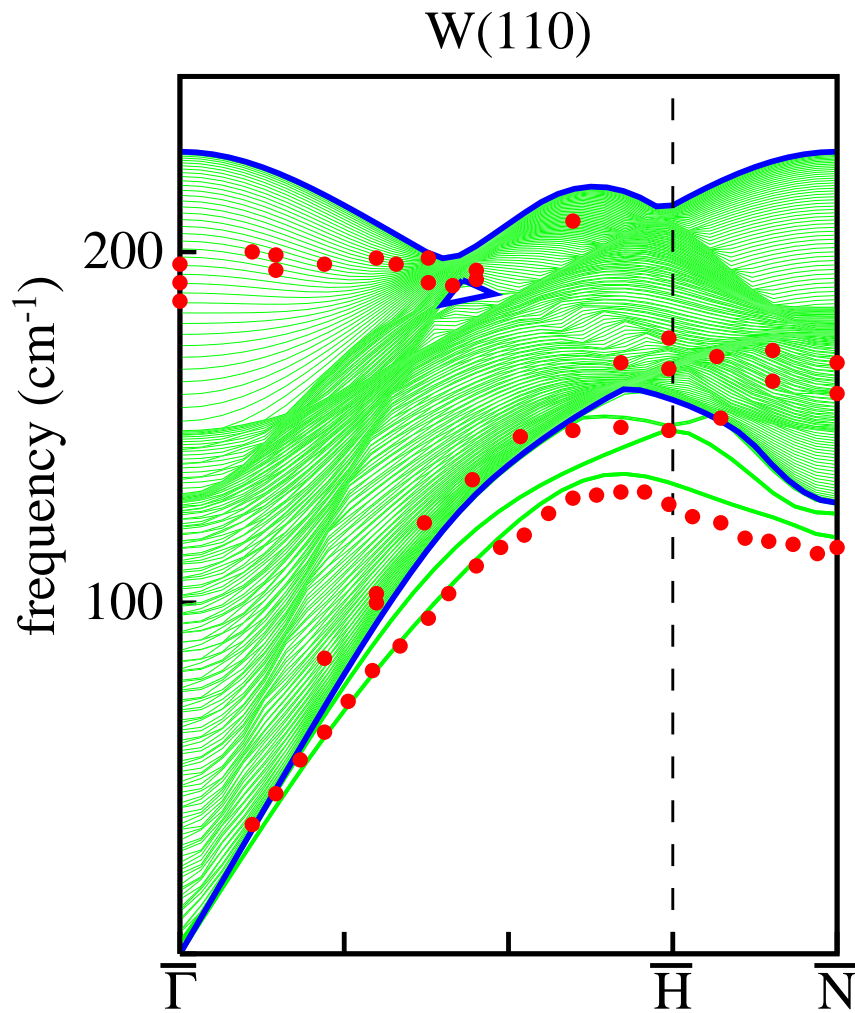


Figure 4.10: Phonon dispersions calculated for a 69 W-layers slab modelling the W(110) surface (green lines). The blue thick lines are the limits of the region of bulk-allowed modes, projected onto the surface BZ. The full dots indicate the experimental EELS data.

at the wave vector \mathbf{q} , α is the polarization index, and the sum runs over the atoms of the two topmost layers of each side of the slab. The localization rate $l_\alpha(\nu, \mathbf{q})$ indicates the percentage of the displacement amplitude along the α direction in the two topmost surface layers for the normal mode ν at the wave vector \mathbf{q} . In Figure 4.11 the modes for which the localization rate is larger than 40% are indicated with full diamonds, one panel for each polarization. We can clearly identify three branches of surface-localized modes, one for each polarization of atomic displacements (displayed in the three panels of Fig. 4.11). Some surface resonance can be also identified at about 170 cm^{-1} and 200 cm^{-1} . The lower branch is a predominantly z-polarized surface mode (Rayleigh mode), whose frequencies are in excellent agreement with the EELS data. The intermediate surface branch is a SH mode (i.e. mainly y-polarized) and therefore it cannot be detected in the experiments. We can identify the third branch of longitudinal (i.e. mainly x-polarized) surface modes with the second branch observed by EELS above the RW mode.

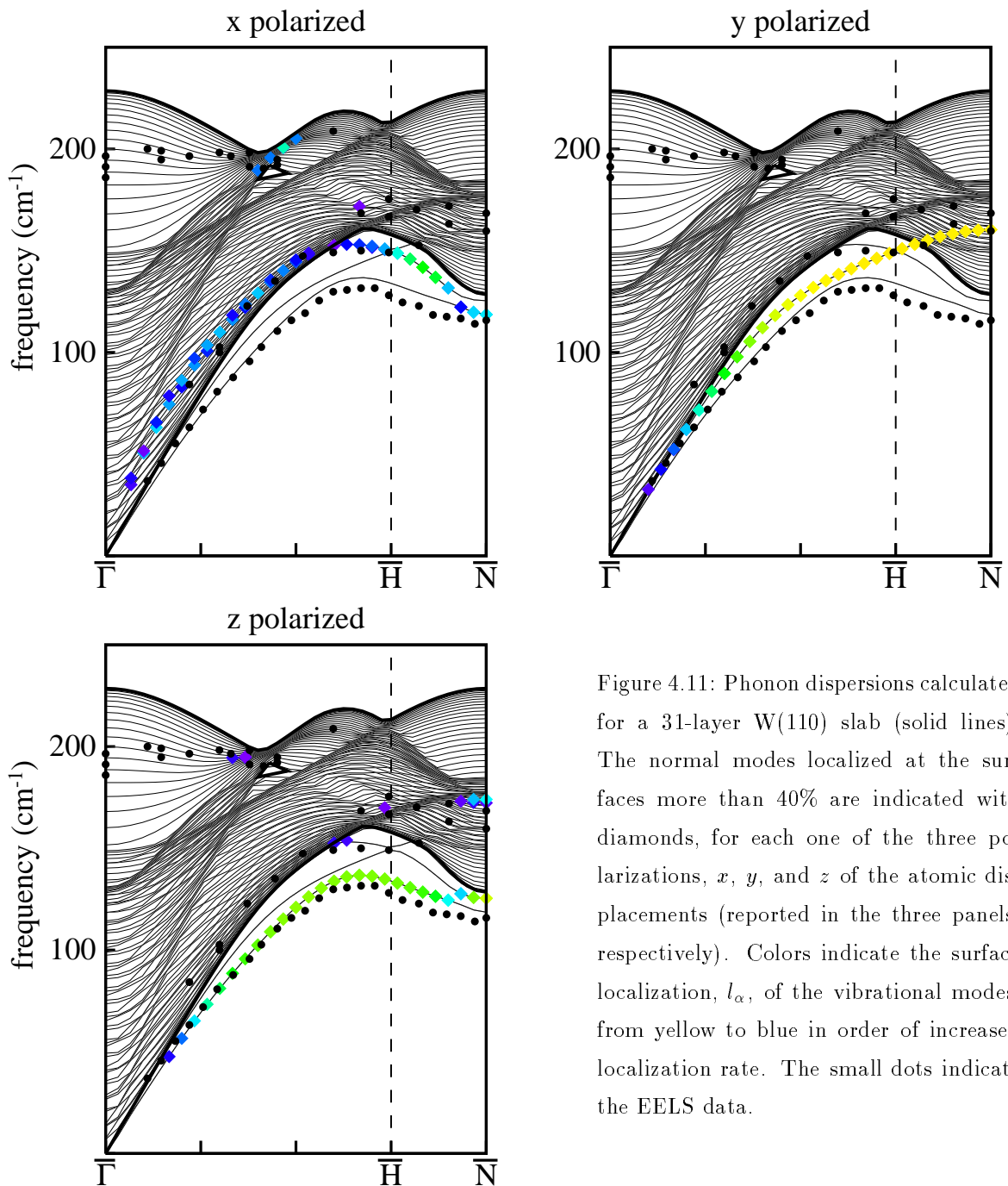


Figure 4.11: Phonon dispersions calculated for a 31-layer W(110) slab (solid lines). The normal modes localized at the surfaces more than 40% are indicated with diamonds, for each one of the three polarizations, x , y , and z of the atomic displacements (reported in the three panels, respectively). Colors indicate the surface localization, l_α , of the vibrational modes: from yellow to blue in order of increased localization rate. The small dots indicate the EELS data.

The EELS spectrum, recorded in the specular direction (i.e. $\mathbf{q} = \bar{\Gamma}$) at low impact energy, shows a dipole active tungsten surface mode at a frequency of about 190 cm^{-1} . The dipole-active surface resonance can be followed up out of Γ within the SBZ. We have not found strongly localized surface modes for any of the three different polarizations corresponding to this surface resonance. We have calculated the surface dipole for each normal mode of the slab, assuming that the dipole moment is proportional to the difference between the displacement amplitude perpendicular to the surface in the first two layers. The results are reported in Fig. 4.12. We interpret the experimental surface resonance at about 190 cm^{-1} as due to dipole surface modes. In the inset of the Fig. 4.12 we show the dipole spectrum calculated at Γ : in very good agreement with the experimental spectrum we have found the maximum dipole intensity at a frequency of 197 cm^{-1} .

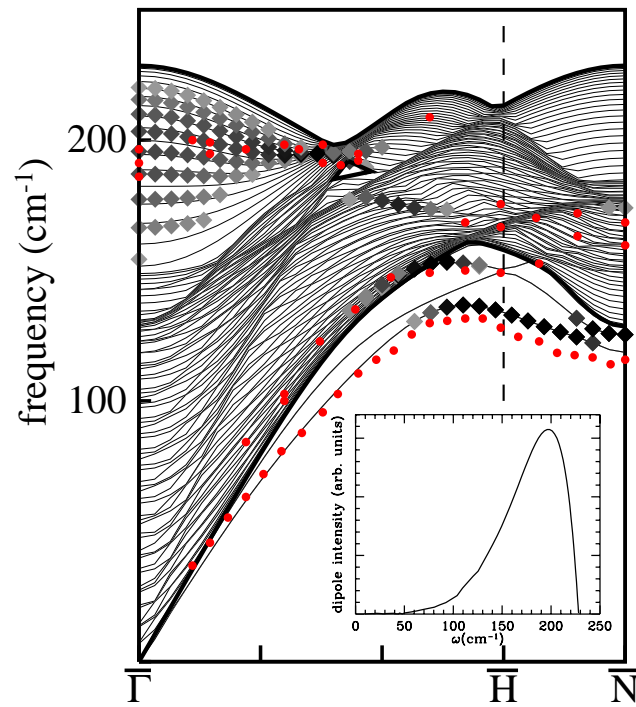


Figure 4.12: Phonon dispersions calculated for a 31 W-layers slab (solid lines). The surface dipole intensity of the modes is indicated with the gray full diamonds. The gray intensity is proportional to the dipole intensity of the vibrational modes. The red small dots indicate the EELS data. In the inset we show the dipole spectrum calculated at $\bar{\Gamma}$.

4.3.2 Hydrogenated surface

The phonon dispersions of the hydrogen-saturated W(110) surface have been calculated along the $\overline{\Gamma\text{H}\text{N}}$ line using a 31-layer W(110) slab with the two equivalent surfaces covered by one layer of hydrogen atoms. The surface force constants are those calculated for the hydrogen-saturated slab of 7 W-layers. The dispersion relations obtained using a broadening width $\sigma=70$ mRy are shown by green lines in the Fig. 4.13. These data do not display any anomaly, but a slight tendency to softening in the RW branch. The calculated dispersion is in very good agreement with the experimental EELS and HAS data, except in the region where the anomalies occur (dashed line), i.e. between $q_x \approx 0.4(2\pi/a)$ and $q_x \approx 0.6(2\pi/a)$. Since the phonon anomalies have a critical dependence upon the broadening width we have studied this dependence in detail. The effect of too large a value of σ is to smooth out the phonon anomalies similarly to what happens at high temperature in real systems. The use of a smaller broadening width requires a finer SBZ sampling and the calculation of the full dynamical matrix of the slab becomes impractical. We have therefore focused our attention on the anomalous RW frequency which is the only one that depends sensitively on σ . The Rayleigh frequency $\omega_\nu(\sigma)$ and the corresponding eigenmode $\mathbf{u}_\nu(\sigma)$ have been calculated by iterative perturbation theory, and considering the dynamical matrix for smaller σ as a perturbation to the matrix calculated for $\overline{\sigma}=70$ mRy. In order to obtain the correction to a given mode, we start from the corresponding lattice distortion, \mathbf{u}_ν , and calculate the electron density response to it using a smaller value of σ . This gives us access directly to a *full*

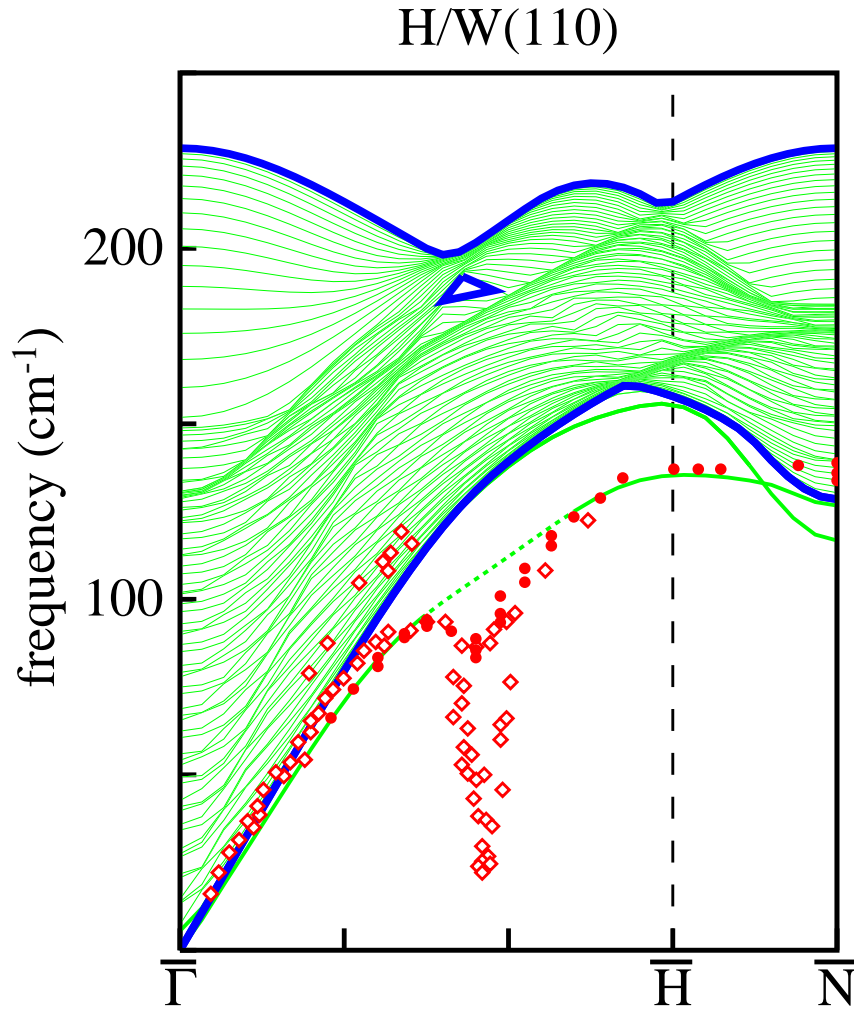


Figure 4.13: Phonon dispersions calculated for a 31-layer W(110) slab, with the two equivalent surfaces saturated by hydrogen atoms (green lines). The blue thick lines indicates the limits of the bulk modes. The red full dots indicate the EELS data, and open diamonds indicate the HAS data. The dashed curve indicates the portion of the phonon branch which is not well converged with the value $\sigma=70$ mRy for the smearing width.

column of the “perturbed” dynamical matrix, $D(\sigma)$:

$$\mathbf{f}_\nu(\sigma) = D(\sigma)|\mathbf{u}_\nu(\bar{\sigma})\rangle. \quad (4.4)$$

Standard perturbation theory allows one to estimate the first-order correction to the frequency:

$$\omega_\nu^2(\sigma) = \langle \mathbf{f}_\nu(\sigma) | \mathbf{u}_\nu(\bar{\sigma}) \rangle + \mathcal{O}((\Delta\sigma)^2), \quad (4.5)$$

and displacement pattern:

$$\Delta\mathbf{u}_\nu^{(1)} = \sum_{\mu \neq \nu} \frac{\langle \mathbf{u}_\mu(\bar{\sigma}) | \mathbf{f}_\nu(\sigma) \rangle}{\omega_\nu^2(\bar{\sigma}) - \omega_\mu^2(\bar{\sigma})} |\mathbf{u}_\mu(\bar{\sigma})\rangle. \quad (4.6)$$

Correspondingly, the second-order correction to the frequency is:

$$\Delta\omega_\nu^{2(2)} = \langle \Delta\mathbf{u}_\nu^{(1)} | \mathbf{f}_\nu(\sigma) \rangle. \quad (4.7)$$

If necessary, the above procedure can be iterated to obtain higher order corrections.

The convergence of the RW mode frequency at the critical wave vector $q_x = 0.45$ ($2\pi/a$) is shown in Table 4.4. The frequency is considerably lowered by reducing σ , and it reaches the converged value of $\approx 76 \text{ cm}^{-1}$ for $\sigma=5$ mRy. Moving away from the critical wave vector the convergence is obtained for larger σ . Outside the critical region the frequencies are already converged for $\sigma=70$ mRy. The RW mode dispersion obtained with $\sigma=10$ mRy is shown in figure 4.14 with the green line and the converged value for the critical wave vector is indicated by the cross. It clearly display an anomalous softening in correspondence to the critical wave vector nesting the Fermi surface of surface-localized states.

The theoretical results are in good agreement with the shallow dip (see Fig. 4.13) observed in both HAS and EELS experiments. This allows us to identify this experimental feature as a Kohn anomaly of the RW mode branch. Our calculations

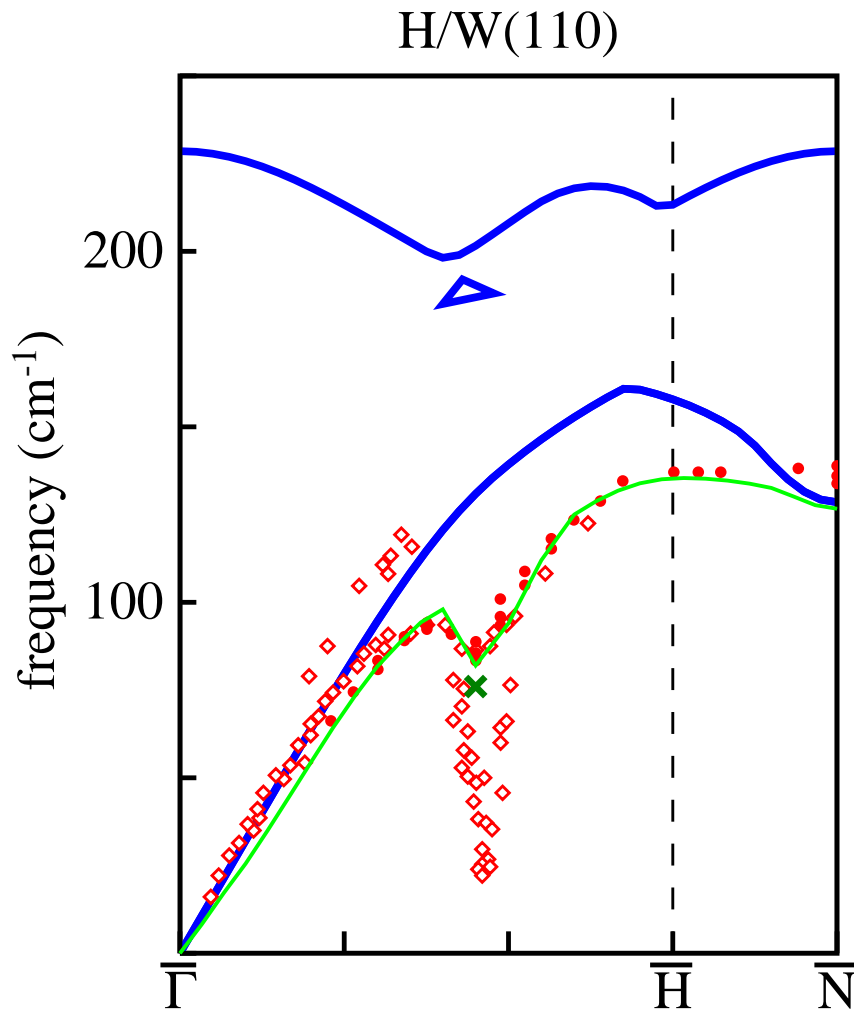


Figure 4.14: Dispersion of the RW mode of the H/W(110) surface, calculated with a broadening width $\sigma=10$ mRy (green line). The cross indicates the converged frequency at the critical wave vector, obtained using a width of 2.5 mRy. The red full dots indicate the experimental EELS data. Open diamonds indicate the HAS data. The blue thick lines are the limits of the region of bulk-allowed modes, projected onto the surface BZ.

Table 4.4: Convergence of the RW mode frequency at the critical wave vector $q_x = 0.45 (2\pi/a)$, with respect to the broadening width, σ , and number of \mathbf{k} -points in the IW of the SBZ, N_k . The experimental value of the shallow dip is also reported as comparison.

σ (mRy)	N_k	ω (cm ⁻¹)	exp. (cm ⁻¹)
70	16	106	83
30	64	96	
10	144	82	
5	324	76	
2.5	324	77	

give a very accurate description of the vibrational properties of bulk W and its (110) surfaces, and to reproduce the anomalous feature in the phonon dispersions, in good agreement with the available experimental data. The calculated dispersions for the H/W(110) do not show any feature comparable with the huge dip found in HAS measurements. On the base of these findings we rule out the interpretation of the deep anomaly as due to adiabatic vibrational excitations, and we suggest that some breakdown of the Born-Oppenheimer approximation should be invoked in order to explain these data.

The surface character of the slab normal modes and their polarization are displayed in Fig. 4.15. The full diamonds indicates, for each polarization, the vibrational modes of the slab that have a localization rate, l_α , larger than 35% over the three surface layers (i.e. the two topmost W-layers and the H-layer).

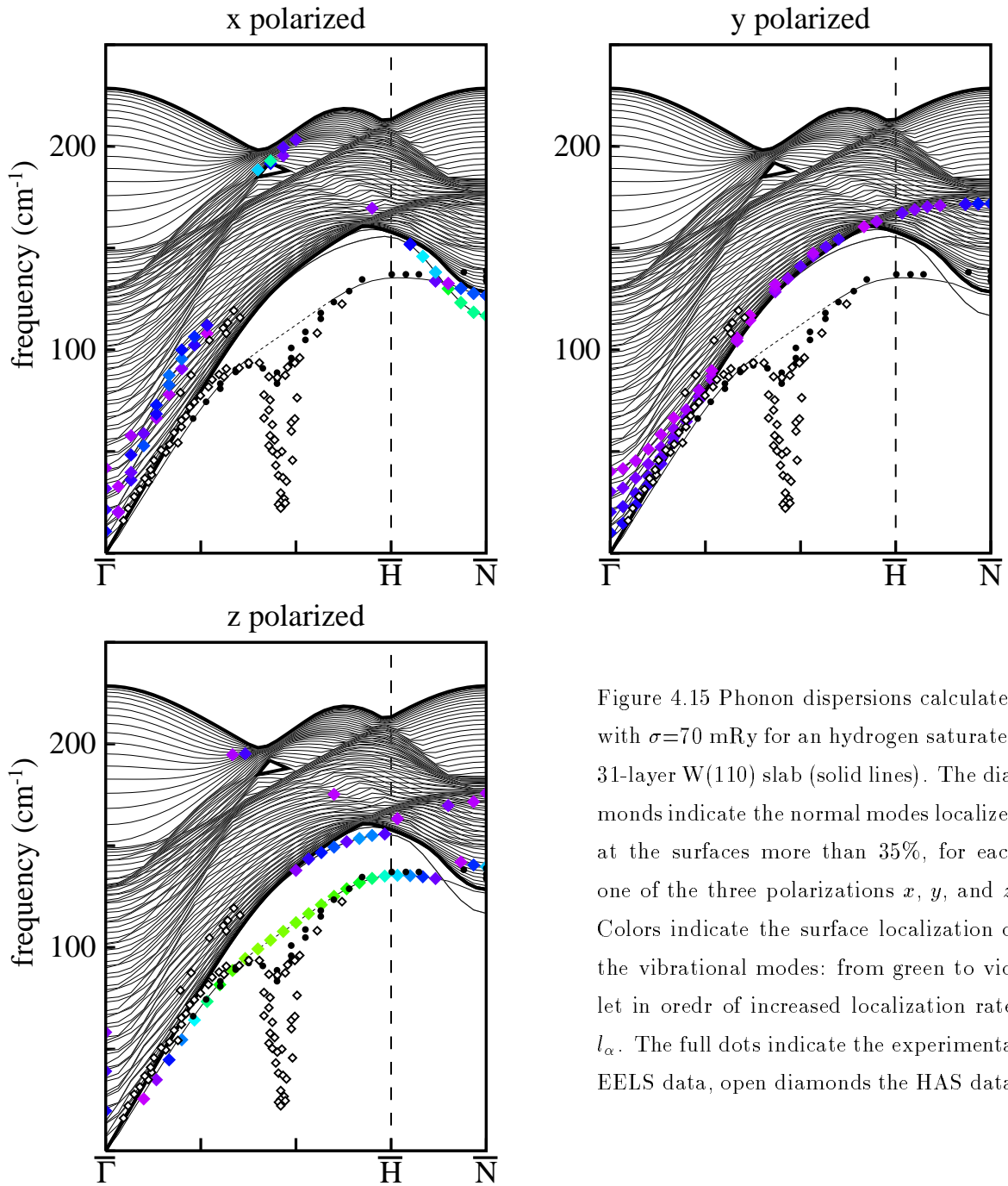


Figure 4.15 Phonon dispersions calculated with $\sigma=70$ mRy for an hydrogen saturated 31-layer W(110) slab (solid lines). The diamonds indicate the normal modes localized at the surfaces more than 35%, for each one of the three polarizations x , y , and z . Colors indicate the surface localization of the vibrational modes: from green to violet in order of increased localization rate, l_{α} . The full dots indicate the experimental EELS data, open diamonds the HAS data.

The lowest surface branch along $\overline{\Gamma\text{H}}$, that is the RW mode (see the panel of z-polarized surface modes in Fig. 4.15), becomes more localized at the surface right in the region of the anomaly. Between $\overline{\text{H}}$ and $\overline{\text{N}}$ the RW branch crosses the longitudinal surface branch, merging at $\overline{\text{N}}$ with bulk allowed modes. In agreement with the experiments, after H-saturation the RW mode of the W(110) surface is essentially unchanged far from the anomaly between $\overline{\Gamma}$ and $\overline{\text{H}}$, and is stiffened between $\overline{\text{H}}$ and $\overline{\text{N}}$. We can identify the upper branch observed in the HAS spectra, as the longitudinal surface resonance (as shown in the panel of x-polarized surface modes in Fig. 4.15). Our calculations show the presence of a third branch of surface-localized SH modes, that cannot be observed in the experiments. The SH mode of the H/W(110) surface is increased in frequency with respect to the SH branch of the clean surface.

Chapter 5

Conclusions

In this thesis we have performed an accurate study of the electronic, vibrational and structural properties of bulk Tungsten and its clean and hydrogenated (110) surfaces. In particular the bulk phonon dispersions result in good agreement with the neutron scattering experimental data, reproducing all the anomalous features of the spectrum. Up to our best knowledge the study presented in this work is the first surface phonon calculation performed from first principles for a metal surface. Our calculations give a very accurate description of the vibrational mode of the clean and H-covered W(110) surfaces, and our surface phonon dispersions are in excellent agreement with the available experimental data. In particular we found an anomalous behavior in the RW mode dispersion of the hydrogen saturated surface in correspondence of the nesting vector connecting parallel portions in the surface localized Fermi surface. The anomalous softening displayed by our RW mode dispersion is in good agreement with the shallow dip detected by HAS and EELS measurements on H/W(110). Due to the nesting features observed in the calculated

Fermi surfaces, the e-ph coupling is kinematically enhanced in correspondence of the nesting vector. Since the electronic states connected by the nesting are well-localized surface states, one expects the phonon modes that are well localized at the surface to be mostly affected by the corresponding Kohn anomaly. The anomalous softening we found in the RW mode is a fingerprint of this enhanced e-ph coupling. On the base of these results we can therefore unambiguously identify the less pronounced experimental anomaly as a Kohn anomaly of the RW mode. The huge dip observed in HAS experiment is not predicted by our results, indicating that it is not an adiabatic phonon excitation. In particular this sharp and pronounced indentation cannot be accounted for by a giant Kohn anomaly of the surface phonon dispersions. We think that this huge anomaly is due to non adiabatic predominantly electron-hole like excitations due to the enhanced electron-phonon coupling occurring at the nesting wave vector. Further calculations of the e-ph coupling will give access to the energy of non-adiabatic excitations allowing us to give a definitive explanation for the origin of the huge dip.

Acknowledgments

First of all I would like to thank my supervisors Stefano Baroni and Stefano de Gironcoli who with their encouragement and continuous suggestions not only introduced me to the research field of this thesis, but also have been a guide in my formation. A special thanks to Sandro Scandolo for the friendly and helpful discussions. Finally I want to thank all those who, although not directly involved in my work, have contributed in creating the friendly atmosphere which I consider essential in any activity.



Appendix A

Smearing technique in Brillouin-zone integration for metals

Calculation of observable quantities such as charge density, forces, interatomic force-constants, etc. . . . , requires integration of periodic functions over \mathbf{k} -vectors in the Brillouin-zone. In the case of metals the functions to be integrated are discontinuous at the Fermi level, due to the partial filling of the energy bands. This fact leads to a very slow convergence with respect to the \mathbf{k} points density, when the integral is evaluated on a uniform mesh in the BZ. On the other hand, the use of a very fine \mathbf{k} -mesh is prohibitive, in practical implementations, for time- and memory-limit reasons. To overcome this problem, Methfessel and Paxton proposed an high-precision scheme for BZ integration in metals [43]. It consists in a modification of the more popular gaussian smearing technique of Fu and Ho [42].

The integrals over the BZ that we wish to evaluate have the following general form

$$I = \int_{BZ} f(\mathbf{k}) \theta(\epsilon_F - \epsilon(\mathbf{k})) d\mathbf{k}, \quad (\text{A.1})$$

where $\epsilon(\mathbf{k})$ represents an energy band as a function of the wave vector, ϵ_F is the Fermi energy, and θ is the step function for the Fermi cutoff:

$$\theta(\epsilon_F - \epsilon(\mathbf{k})) = \int_{-\infty}^{\epsilon_F} \delta(\epsilon - \epsilon(\mathbf{k})) d\epsilon. \quad (\text{A.2})$$

The \mathbf{k} -convergence can be easily improved by broadening the δ function in eq. A.2 into Gaussian, Lorentzian or similar smooth functions with characteristic linewidth σ . In fact, provided that the average energy separation between neighboring computed eigenvalues is small with respect to σ , the discontinuity arising from the step function is smeared out, and the integral can be computed accurately on a discrete grid of points in the BZ.

However the only justification for this *ad hoc* procedure is that in the limit $\sigma \rightarrow 0$ one recovers the absolutely converged result at the expense of using a prohibitively fine mesh. Thus, for each choice of σ , the \mathbf{k} -sum converges to a different value, and convergence with respect to the broadening width σ must be further checked.

Methfessel and Paxton suggested an efficient way to achieve absolute convergence, based on a more sophisticated choice of the broadening function. They expand the delta function as:

$$\delta(x) = \sum_{n=0}^{\infty} A_n H_{2n}(x) e^{-x^2} \quad (\text{A.3})$$

where $x = \frac{\epsilon - \epsilon(\mathbf{k})}{\sigma}$, H_{2n} are Hermite polynomials, A_n are the expansion coefficients, and σ is an arbitrary "linewidth".

By truncating the sum in eq. A.3 to a finite order N one obtains a broadened $\tilde{\delta}$ -function and a corresponding smooth approximation $\tilde{\theta}$ for the step function A.2.

The order $N = 0$ corresponds to the simple gaussian broadening [42]. By construction, truncation to the finite order N leads to a negligible error in the evaluation of the integral A.1, if the function f is representable as a polynomial of degree $2N$ or less in an interval of $\sim 5\sigma$ around the Fermi energy. The \mathbf{k} -converged result can therefore be made to approach the true value either by increasing N or by reducing σ . Unless f is a constant near the Fermi level, the simple gaussian smearing gives results considerably far from the desired *zero-width* limit, and a good convergence is obtained only for a very small linewidth. In many instances, the first-order approximation ($N=1$) in the smearing function is enough to have a significant enhancement in precision with a minimal extra effort in the BZ sampling (see reference [16]), and satisfactory converged results can be obtained using a broadening width of $\sim 1eV$.

Bibliography

- [1] A review on surface phonon can be found in: G. Benedek and J.P. Toennies, Surf. Sci. **299/300**, 588 (1994); J.P. Toennies Superlatt. and Microstr. **7**, 193 (1990); K. Kress, F.W. de Wette, *Surface Phonons*, Springer Verlag (Berlin, 1991).
- [2] E. Hulpke and J. Ludecke, Surf. Sci. **272**, 289 (1992). .
- [3] E. Hulpke and J. Ludecke, Phys. Rev. Lett. **68**, 2846 (1992).
- [4] E. Hulpke and J. Ludecke, Surf. Sci. **287-188**, 837 (1993).
- [5] E. Hulpke and J. Ludecke, J. Electron. Spectr. Relat. Phenom. **64/65**, 641 (1993).
- [6] M. Balden, S. Lehwald, E. Preuss, H. Ibach, Surf. Sci. **307-309**, 1141 (1994).
- [7] B. Renker, H. Rietschel, L. Pintschovius, W. Gläser, P. Brüesch, D. Kuse, M.J. Rice, Phys. Rev. Lett. **30**, 1144 (1973).
- [8] P. Brüesch:*Phonons: Theory and Experiments III*, Springer Ser. Solid-State Sci., Vol. 66, p.108, (Springer, Berlin, Heidelberg 1986).

-
- [9] K. Jeong, R.H. Gaylord, and S.D. Kevan, *J. Vac. Sci. Technol. A* **7**, 2199 (1989);
R.H. Gaylord, K. Jeong, S. Dhar, and S.D. Kevan, *J. Vac. Sci. Technol. A* **7**,
2203 (1989).
- [10] H.-J. Ernst, E. Hulpke, and J.P. Toennies, *Phys. Rev. Lett.* **58**, 1941 (1987);
Europhys. Lett. **10**, 747 (1989); E. Hulpke and D.-M. Smilgies, *Phys. Rev. B*
40, 1338 (1989).
- [11] E. Tosatti, *Solid State Commun.* **25**, 637 (1978); A. Fasolino and E. Tosatti,
Phys. Rev. B **35**, 4264 (1987).
- [12] P. Giannozzi, S. de Gironcoli, P. Pavone and S. Baroni, *Phys. Rev. B* **43**, 7231
(1991).
- [13] M. Buongiorno Nardelli, S. Baroni, and P. Giannozzi, *Phys. Rev. Lett.* **69**, 1069
(1992).
- [14] S. Baroni, S. de Gironcoli, and P. Giannozzi, *Phys. Rev. Lett.* **65**, 84 (1990).
- [15] S. Baroni, P. Giannozzi, and E. Molinari, *Phys. Rev. B* **41**, 3870 (1990).
- [16] S. de Gironcoli, *Phys. Rev. B* **51**, 6773 (1995).
- [17] J. Fritsch, P. Pavone, and U. Schröder, *Phys. Rev. Lett.* **71**, 4194 (1993).
- [18] R.J. Smidth, C. Hrnnessy, M.W. Kim, C.N. Whang, M. Worthington, and Xu
Mingde, *Phys. Rev. Lett.* **58**, 702 (1987).
- [19] V.V. Gonchar, Yu. M. Kagan, O.V. Kanash, A.G. Naumovets, and A.G. Fe-
dorus, *Sov. Phys. JETP* **57**, 142 (1983).

-
- [20] J.W. Chung, S.C. Ying, and P.J. Estrup, Phys. Rev. Lett. **56**, 749 (1986).
- [21] G.B. Blanchet, N.J. DiNardo, and E.W. Plummer, Surf. Sci. **118**, 496 (1982).
- [22] M. Balden, S. Lehwald, H. Ibach, and D.L. Mills, Phys. Rev. Lett. **73**, 854 (1994).
- [23] E. Tosatti, to be published in: *Electronic Surface and Interface States on Metallic Systems*, Eds. E. Bertel and M. Donath (World Scientific, Singapore, 1995).
- [24] P.A. Lee, T.M. Rice, and P.W. Anderson, Solid State Commun. **14**, 703 (1974).
- [25] B. Kohler, P. Ruggerone, M. Scheffler, and E. Tosatti, to be published.
- [26] B. Kohler, P. Ruggerone, S. Wilke, and M. Scheffler, Phys. Rev. Lett. **74**, 1387 (1995).
- [27] M. Born and K. Huang, *Dynamical Theory of Crystal Lattices* (Oxford, Clarendon Press, 1954).
- [28] P. Hohenberg and W. Kohn, Phys. Rev. **136**, B864 (1964).
- [29] W. Kohn and L.J. Sham, Phys. Rev. **140**, A1133 (1965).
- [30] D.R. Hamann and M. Schlüter, and C. Chiang, Phys. Rev. Lett. **46**, 1494 (1979).
- [31] G.B. Bachelet, D.R. Hamann and M. Schlüter, Phys. Rev. B **26**, 4199 (1982).
- [32] G.P. Kerker, J. Phys. C **13**, L189 (1980).
- [33] N. Troullier, and J.L. Martins, Phys. Rev. B **43**, 1993 (1991).

-
- [34] G.B. Bachelet and N.C. Christensen, *Phys. Rev. B* **8**, 5747 (1973).
- [35] W.E. Pickett, *Comp. Phys. Rep.* **9**, 115 (1989).
- [36] L. Kleinman, and D.M. Bylander, *Phys. Rev. Lett.* **48**, 1425 (1982).
- [37] X. Gonze, P. Käckell, and M. Scheffler *Phys. Rev. B* **41**, 12264 (1990).
- [38] H. Böttger, *Principles of the Theory of Lattice Dynamics* (Berlin, Akademie-Verlag, 1983).
- [39] X. Gonze, and J.P. Vigneron, *Phys. Rev. B* **39**, 13120 (1989).
- [40] R.P. Feynman, *Phys. Rev.* **56**, 340 (1939).
- [41] S. Baroni, P. Giannozzi and A. Testa, *Phys. Rev. Lett* **58**, 1861 (1987).
- [42] C.L. Fu, and K.M. Ho, *Phys. Rev. B* **28**, 5480 (1983).
- [43] M. Methfessel, and A.T. Paxton, *Phys. Rev. B* **40**, 3616 (1989).
- [44] H.J. Monkhorst and J.D. Pack, *Phys. Rev. B* **13**, 5188 (1976).
- [45] J. Perdew, and A. Zunger, *Phys. Rev. B* **23**, 5048 (1981).
- [46] C.J. Smithells, *Smithells metals reference book*, E.A. Brandes, London, Butterworths (1983).
- [47] C.M. Varma and W. Weber, *Phys. Rev. Lett.* **39**, 1094 (1977).
- [48] C.M. Varma and W. Weber, *Phys. Rev. B* **19**, 6142 (1979).
- [49] T.M. Rice and B.I. Halperin, *Phys. Rev. B* **1**, 509 (1979).

-
- [50] W. Kohn, Phys. Rev. Lett. **2**, 393 (1959).
- [51] R. Landolt-Börnstein Series, *Metals: phonon states, electron states and Fermi surfaces*, Vol. 13a, Group. III, Eds. K.H.Hellwedge and J.H. Olson (Springer, Berlin 1981).
- [52] S.L. Cunningham, Phys. Rev. B **10**, 4988 (1974).
- [53] W.H. Press *et al.*, *Numerical Recipes*, Cambridge University Press (Cambridge 1986).
- [54] R. Landolt-Börnstein New Series, *Physics of solid surfaces: structure*, Vol. 24a, Group. III, Ed. G. Chiarotti (Springer, Berlin 1993).
- [55] A.M. Afanas'ev and Yu. Kagan, Sov. Phys. JETP **16**, 1030 (1963).
- [56] J.A. Wilson, F.J. Di Salvo, and S. Mahajan, Phys. Rev. Lett. **32**, 882 (1974); G. Benedek, G. Brusdeylins, C. Heimlich, L. Miglio, J.G. Skofronick, J.P. Toennies, R. Vollmer, Phys. Rev. Lett. **60**, 1037 (1988).
- [57] A. Baldereschi, S. Baroni, and R. Resta, Phys. Rev. Lett. **61**, 734 (1988).
- [58] B.D. Bardford and R.R. Rye, J. Chem. Phys. **60**, 1046 (1974).
- [59] R.W. Strayer, W. Mackie, and L.W. Swanson, Surf. Sci. **34**, 225 (1973).
- [60] For a review on surface phonons see: Springer series in surface sciences Vol. 21: "*Surface Phonons*", Eds. W. Kress and F.W. de Wette, (Springer, Berlin 1991). .

- [61] M. Balden, S. Lehwald, and H. Ibach, *Phys. Rev. B* **46**, 4172 (1992).